On the breakdown of boundary layer streaks

By PAUL ANDERSSON[1]†, LUCA BRANDT[1],
ALESSANDRO BOTTARO[2] AND DAN S. HENNINGSON[1]†

[1] Department of Mechanics, Royal Institute of Technology (KTH), S-100 44 Stockholm, Sweden
[2] Institut de Mécanique des Fluides de Toulouse (IMFT), Université Paul Sabatier,
118 route de Narbonne, 31062 Toulouse Cedex 4, France

A scenario of transition to turbulence likely to occur during the development of natural disturbances in a flat-plate boundary layer is studied. The perturbations at the leading edge of the flat plate that show the highest potential for transient energy amplification consist of streamwise aligned vortices. Due to the lift-up mechanism these optimal disturbances lead to elongated streamwise streaks downstream, with significant spanwise modulation. Direct numerical simulations are used to follow the nonlinear evolution of these streaks and to verify secondary instability calculations. The theory is based on a linear Floquet expansion and focuses on the temporal, inviscid instability of these flow structures. The procedure requires integration in the complex plane, in the coordinate direction normal to the wall, to properly identify neutral modes belonging to the discrete spectrum. The streak critical amplitude, beyond which streamwise travelling waves are excited, is about 26% of the free-stream velocity. The sinuous instability mode (either the fundamental or the subharmonic, depending on the streak amplitude) represents the most dangerous disturbance. Varicose waves are more stable, and are characterized by a critical amplitude of about 37%. Stability calculations of streamwise streaks employing the shape assumption, carried out in a parallel investigation, are compared to the results obtained here using the nonlinearly modified mean fields; the need to consider a base flow which includes mean flow modification and harmonics of the fundamental streak is clearly demonstrated.

1. Introduction

1.1. *'Lift-up' effect and transient growth*

For quite a long time the fluid mechanics community has recognized transition to turbulence as a fundamental problem and has directed intense research efforts toward its understanding. Even so, our current picture of the physical processes involved is far from complete. The classical starting point for theoretical investigations of transition is linear stability theory. Here, exponentially growing solutions – in time or space – to the linearized Navier–Stokes equations are sought. If such solutions are not found, the flow is predicted by the theory to be stable. However, experiments show that the route to turbulence is highly dependent on the initial conditions and on the continuous forcing that background noise can provide (see for example Morkovin & Reshotko 1990 and Reshotko 1994 for reviews).

† Also at the Aeronautical Research Institute of Sweden (FFA), Box 11021, S-161 11 Bromma, Sweden.

Experiments reveal that many flows, including for example Poiseuille and boundary layer flows, may undergo transition to turbulence for Reynolds numbers well below the critical ones from the linear stability theory. For the case of plane Couette flow the theory predicts stability at all Reynolds numbers (Romanov 1973) while numerical and laboratory experiments point to a finite transitional value (Lundbladh & Johansson 1991; Tillmark & Alfredsson 1992; Dauchot & Daviaud 1995).

The reason for this discrepancy between the theory and the experiments has been sought in the nonlinear terms of the Navier–Stokes equations. Examples of nonlinear theories are given by Orszag & Patera (1983), Bayly, Orszag & Herbert (1988) and Herbert (1988). However, examining the Reynolds–Orr equation (Drazin & Reid 1981) a remarkably strong statement can be made on the nonlinear effects: the nonlinear terms redistribute energy among disturbance frequencies but have no net effect on the instantaneous growth rate of the energy. This implies that there must exist a linear growth mechanism for the energy of a disturbance of any amplitude to increase (Henningson & Reddy 1994; Henningson 1996). The apparent need for an alternative growth mechanism based on the linearized equations has recently led to intense re-examination of the classical linear stability theory.

The first convincing alternative was proposed by Ellingsen & Palm (1975). By introducing an infinitesimal disturbance without streamwise variation in a shear layer, they showed that the streamwise velocity component can increase linearly with time, within the inviscid approximation, producing alternating low- and high-velocity streaks in the streamwise velocity component. Landahl (1975, 1980) extended this result to the linear evolution of localized disturbances and supplied the physical insight to the linear growth mechanism with what he denoted the *lift-up* effect. He argued that vortices aligned in the streamwise direction advect the mean velocity gradient towards and away from the wall, generating spanwise inhomogeneities.

It is now clear that since the linearized Navier–Stokes operator is non-normal for many flow cases (e.g. shear flows) a significant transient growth of a given perturbation might occur, before the subsequent exponential behaviour. Such an algebraic growth involves non-modal perturbations and can exist for subcritical values of the governing parameters.

Indeed, early investigators of the lift-up and transient growth mechanisms found considerable linear energy amplification before the viscous decay (Hultgren & Gustavsson 1981; Boberg & Brosa 1988; Gustavsson 1991; Butler & Farrell 1992; Reddy & Henningson 1993; Henningson, Lundbladh & Johansson 1993). An overview of recent work can be found in the review articles by Trefethen et al. (1993) and Henningson (1995). The initial disturbance that yields the maximum spatial transient growth in a non-parallel flat-plate boundary layer flow was determined independently by Andersson, Berggren & Henningson (1999a) and Luchini (2000) to consist of vortices aligned in the streamwise direction. These vortices leave an almost permanent scar in the boundary layer in the form of long-lived, elongated streaks of alternating low and high streamwise speed.

1.2. *'Secondary' instability of streamwise streaks*

If the amplitude of the streaks grows to a sufficiently large value, instabilities can develop which may provoke early breakdown and transition despite the theoretically predicted modal decay. In the remainder of the paper we will refer to the instability of the streak as a 'secondary' instability, to differentiate it from the 'primary' growth mechanism responsible for the formation of these flow structures. A (secondary) instability can be induced by the presence of inflection points in the base flow velocity

profile, a mechanism which does not rely on the presence of viscosity. Controlled experiments on the breakdown of periodically arranged (along the span) streaks produced by an array of roughness elements have been conducted by Bakchinov *et al.* (1995). It was shown that the instability of the streaks causes transition in a similar manner as do the Görtler and cross-flow cases, i.e. via amplification of the secondary wave up to a stage where higher harmonics are generated, and on to a destruction of the spanwise coherence of the boundary layer. Alfredsson & Matsubara (1996) considered the case of transition induced by streaks formed by the passage of fluid through the screens of the wind-tunnel settling chamber. They report on the presence of a high-frequency 'wiggle' of the streak with a subsequent breakdown into a turbulent spot.

Today, the description of the establishment of steady streaky structures is well captured by the theory. The work presented here aims at understanding the instability of these streaks on the path to boundary layer turbulence. Parenthetically, we note also that streamwise vortices and streaks are an essential ingredient of the near-wall turbulent boundary layer and that the instability of streaky structures is one crucial feature of the near-wall cycle which is thought to lie at the heart of the genesis and dynamics of turbulent coherent structures (Jimenez & Pinelli 1999; Schoppa & Hussain 1997, 1998).

Some work has recently appeared in the literature on the instability of streaks in channel flows (Waleffe 1995, 1997; Reddy *et al.* 1998) and, among the findings reported, it is interesting to note that slip and no-slip boundaries do not display significant differences in the instability scenario (Waleffe 1997). The present study focuses on the linear, inviscid breakdown of boundary layer streaks. It is believed that the inviscid approximation captures the essential features of the breakdown. This is supported primarily by the controlled experiments of Bakchinov *et al.* (1995), who demonstrate unambiguously the role of the critical layer in the development of the instability. The measurements conducted by Boiko *et al.* (1997) on the instability of a vortex in a boundary layer and the very carefully controlled experiments on the breakdown of streaks in channel flow conducted by Elofsson, Kawakami & Alfredsson (1999) further attest to the inflectional nature of the breakdown. The latter authors generated elongated streamwise streaky structures by applying wall suction, and triggered a secondary instability by the use of earphones. The growth rate of the secondary instability modes was unaffected by a change of the Reynolds number of their flow, over a subcritical range, and the regions of (sinuous-type) oscillations of the streaks in cross-stream planes were reasonably well correlated with the spanwise shear of the main flow. The numerical/theoretical comparative viscous–inviscid investigations on the linear breakdown of longitudinal vortices in a curved channel (Randriarifara 1998) and the numerous studies on the secondary instability of Görtler vortices (Hall & Horseman 1991; Yu & Liu 1991; Bottaro & Klingmann 1996), show that the inviscid approach captures correctly the dominant features of the instability with viscosity playing mainly a damping role. These secondary instability studies bear a close resemblance to the present one.

1.3. *Mean field with optimal streaks and linear stability analysis*

The equations governing the streak evolution are obtained by applying the boundary layer approximations to the three-dimensional steady incompressible Navier–Stokes equations and linearizing around the Blasius base flow. After defining the disturbance energy density as the integral, in the wall-normal direction, of the square of the disturbance velocity components, techniques commonly employed when solving
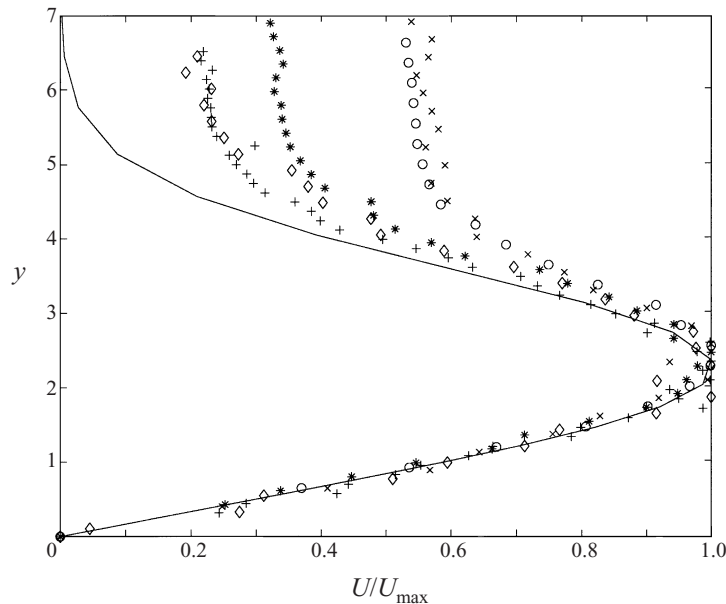
FIGURE 1. Comparison between the streamwise velocity component of the downstream response to an optimal perturbation, and the *u*-r.m.s. data in a flat-plate boundary layer subject to free-stream turbulence (——, Reynolds-number-independent theory). The symbols represent experiments from Westin *et al.* (1994) (○, $Re_\delta = 203$; +, $Re_\delta = 233$; ×, $Re_\delta = 305$; *, $Re_\delta = 416$; ◇, $Re_\delta = 517$). Here y has been made non-dimensional – and the Reynolds number is defined – using the Blasius length scale $\delta = (Lv/U_\infty)^{1/2}$.

optimal control problems are used to determine the optimal disturbance (streamwise oriented vortices) and its downstream response (streamwise streak). The output streak predicted by the theory of Andersson *et al.* (1999*a*) and Luchini (2000) is remarkably similar to that measured in the laboratory (see figure 1). The measurements were performed in a pre-transitional flat-plate boundary layer, where the largest amplitude of the streamwise velocity was 11% of the free-stream velocity. The streak is, in fact, a 'pseudo-mode' triggered in a flat-plate boundary layer subject to significant outside disturbances.

The instability of these optimal streaks is studied here with different levels of approximation. Two different representations are used for the mean field: the simpler shape assumption, where the shape of the streak obtained from the linearized equations is considered unmodified even at large amplitudes, and the complete nonlinear development of the streak.

In both formulations the linear secondary stability calculations are carried out on the basis of the boundary layer approximation, i.e. the mean field to leading order will consist only of the streamwise velocity component (here denoted U), consistent with the scaling hypothesis which led to the definition of the streak. Such a mean field varies on a slow streamwise scale, whereas the secondary instability varies rapidly in the streamwise direction x, as observed in the visualizations by Alfredsson & Matsubara (1996). Hence, our leading-order stability problem is the parallel flow problem, with perturbation mode shapes dependent only on the cross-stream coordinates y (wall-normal) and z (spanwise). The same approximation was made previously for the case of the Görtler flow (Hall & Horseman 1991; Yu & Liu 1991; Bottaro & Klingmann 1996).

Due to the spanwise periodicity of the base flow – consisting of streamwise aligned streaks superimposed on a flat-plate Blasius flow – a temporal Floquet analysis is employed with the objective of determining which disturbance pattern shows the highest potential for temporal growth. In particular we are interested in determining if the maximum disturbance growth occurs for a sinuous or a varicose disturbance, and whether it is of fundamental or subharmonic type. In addition, the critical threshold amplitude of the streak for the onset of the secondary instability is determined.

In §2 the two-dimensional eigenvalue problem arising from the governing partial differential equation is formulated and the numerical methods adopted are described. In §3 a scaling property of the mean field calculated by nonlinear simulations is introduced; this property allows a reduced number of simulations to cover a wide range of spanwise scales of the disturbance. Numerical experiments on streak instability are also carried out using DNS and the results are compared with the linear stability calculations. In §4 a parametric study of the sinuous modes is presented and some comparisons with the shape assumption calculations are discussed. The main conclusions of the work are summarized in §5.

2. Governing equations and numerical methods

2.1. *Inviscid stability equations*

The dimensionless, incompressible Euler equations linearized around the mean field $(U(y,z), 0, 0)$ are

$$u_x + v_y + w_z = 0, \tag{2.1}$$

$$u_t + Uu_x + U_y v + U_z w = -p_x, \tag{2.2}$$

$$v_t + Uv_x = -p_y, \tag{2.3}$$

$$w_t + Uw_x = -p_z, \tag{2.4}$$

and the system is closed by slip boundary conditions at the solid wall and by decaying disturbances in the free stream; $(u, v, w) = (u(x, y, z, t), v(x, y, z, t), w(x, y, z, t))$ are the perturbation velocities in the streamwise, wall-normal and spanwise directions, respectively, t is time and $p = p(x, y, z, t)$ is the disturbance pressure. All velocities have been scaled with the free-stream speed U_∞ and the pressure with ρU_∞^2, where ρ is the fluid density. The length scale is $\delta = (Lv/U_\infty)^{1/2}$, with v kinematic viscosity and L distance from the leading edge. For later use we define two Reynolds numbers using the two different length scales, $Re_\delta = U_\infty \delta/v$ and $Re = U_\infty L/v$, which relate as $Re = Re_\delta^2$.

The presence of both wall-normal and spanwise gradients in the mean field makes it impossible to obtain an uncoupled equation for either of the velocity components. It is, however, possible to find an uncoupled equation for the pressure by taking the divergence of the momentum equations, introducing continuity and then applying equations (2.3) and (2.4) (Henningson 1987; Hall & Horseman 1991). These manipulations yield

$$\left(\frac{\partial}{\partial t} + U \frac{\partial}{\partial x}\right) \Delta p - 2U_y p_{xy} - 2U_z p_{xz} = 0. \tag{2.5}$$

We consider perturbation quantities consisting of a single wave component in the streamwise direction, i.e.

$$p(x, y, z, t) = \text{Re} \{\tilde{p}(y, z) e^{i\alpha(x-ct)}\},$$

where α is the (real) streamwise wavenumber and $c = c_r + \mathrm{i} c_i$ is the phase speed. The equation governing the pressure reduces to

$$(U - c)\left(\frac{\partial^2}{\partial y^2} + \frac{\partial^2}{\partial z^2} - \alpha^2\right)\tilde{p} - 2U_y\tilde{p}_y - 2U_z\tilde{p}_z = 0; \tag{2.6}$$

this constitutes a generalized eigenproblem with c in the role of eigenvalue and needs to be solved for given mean field and streamwise wavenumber. Once the pressure eigenfunctions are computed, the velocity components can be obtained from the explicit expressions

$$\mathrm{i}\alpha(U - c)\tilde{v} = -\tilde{p}_y, \tag{2.7}$$

$$\mathrm{i}\alpha(U - c)\tilde{w} = -\tilde{p}_z, \tag{2.8}$$

$$\mathrm{i}\alpha(U - c)\tilde{u} + U_y\tilde{v} + U_z\tilde{w} = -\mathrm{i}\alpha\tilde{p}. \tag{2.9}$$

The pressure component $\tilde{p}$ is expanded in an infinite sum of Fourier modes

$$\tilde{p}(y, z) = \sum_{k=-\infty}^{\infty} \hat{p}_k(y)\mathrm{e}^{\mathrm{i}(k+\gamma)\beta z}, \tag{2.10}$$

where β is the spanwise wavenumber of the primary disturbance field and γ is the (real) Floquet exponent. We note two symmetries: first, to within renumbering of the Fourier coefficients γ and $\gamma \pm n$ yield identical modes for any integer n, and second, equation (2.6) is even under the reflection $z \to -z$. These symmetries make it sufficient to study values of γ between zero and one half, with $\gamma = 0$ corresponding to a *fundamental* instability mode, and $\gamma = 0.5$ corresponding to a *subharmonic* mode (see Herbert 1988 for a thorough discussion on fundamental and detuned instability modes). The mean field is also expanded as a sum of Fourier modes

$$U(y, z) = \sum_{k=-\infty}^{\infty} U_k(y)\mathrm{e}^{\mathrm{i}k\beta z} \tag{2.11}$$

and these expansions are introduced into equation (2.6) to yield an equation that holds for each integer k:

$$\sum_{j=-\infty}^{\infty}\left(U_{k-j}\left[\frac{\partial^2}{\partial y^2} - \beta^2(j+\gamma)^2 - \alpha^2\right] - 2\frac{\partial U_{k-j}}{\partial y}\frac{\partial}{\partial y} + 2\beta^2(k-j)(j+\gamma)U_{k-j}\right)\hat{p}_j$$

$$= c\left[\frac{\partial^2}{\partial y^2} - \beta^2(k+\gamma)^2 - \alpha^2\right]\hat{p}_k. \tag{2.12}$$

The appropriate boundary conditions are

$$\frac{\partial\hat{p}_k}{\partial y} = 0 \quad \text{at} \quad y = 0 \quad \text{and} \quad \frac{\partial\hat{p}_k}{\partial y} \to 0 \quad \text{when} \quad y \to \infty. \tag{2.13}$$

This problem consists of an infinite number of coupled ordinary differential equations which must be truncated in order to find a numerical solution. The complete system must be solved numerically, when the solution is sought for an arbitrary value of the detuning parameter γ. If, however, even and odd solutions in z are sought, the system of equations can be simplified for the fundamental and subharmonic modes. In this case the numerical effort is decreased considerably because the dimension of the matrices arising from the discretization is halved.

In the fundamental ($\gamma = 0$) case, even (odd) modes are obtained by imposing the condition $\hat{p}_{-k} = \hat{p}_k$ ($\hat{p}_{-k} = -\hat{p}_k$). This is equivalent to introducing either a cosine or a sine expansion

$$\tilde{p}(y,z) = \sum_{k=0}^{\infty} \hat{p}_k(y) \cos(k\beta z), \tag{2.14}$$

$$\tilde{p}(y,z) = \sum_{k=1}^{\infty} \hat{p}_k(y) \sin(k\beta z), \tag{2.15}$$

into equation (2.6), to yield two different systems of ODEs.

In the case of subharmonic disturbances ($\gamma = 0.5$) the spanwise periodicity of the fluctuations is twice that of the base flow. The subharmonic mode also contains a symmetry which renders the decoupling into even and odd modes possible. In this case the cosine and sine expansions are

$$\tilde{p}(y,z) = \sum_{k=0}^{\infty} \hat{p}_k(y) \cos\left(\frac{2k+1}{2}\beta z\right), \tag{2.16}$$

$$\tilde{p}(y,z) = \sum_{k=0}^{\infty} \hat{p}_k(y) \sin\left(\frac{2k+1}{2}\beta z\right). \tag{2.17}$$

These two expansions produce two new systems of ODEs which clearly yield two different classes of solutions, as in the case of the fundamental modes. Notice, however, that the sinuous fluctuations of the low-speed streaks, represented in the fundamental case by the sine expansion (2.15) are given, in the subharmonic case, by the cosine expansion (2.16). This is because the subharmonic sinuous case treats two streaks, which oscillate out of phase (cf. Le Cunff & Bottaro 1993). Likewise, varicose oscillations of the low-speed streaks are represented by the cosine series (2.14) for the fundamental mode, and by the sine expansion (2.17) in the case of subharmonic perturbations.

For the sake of clarity, in the remainder of the paper only the definitions of *sinuous* or *varicose* modes of instability will be employed, with reference to the visual appearance of the motion of the *low-speed streaks*. A sketch of the different fundamental and subharmonic modes is provided in figure 2: it clearly illustrates how in the subharmonic cases sinuous (varicose) fluctuations of the low-speed streaks are always associated with staggered (in x) varicose (sinuous) oscillations of the high-speed streaks.

2.2. *Chebyshev polynomials in real space*

The temporal eigenvalue system derived in §2.1 is solved numerically using a spectral collocation method based on Chebyshev polynomials. Consider the truncated Chebyshev expansion

$$\phi(\eta) = \sum_{n=0}^{N} \bar{\phi}^n T_n(\eta),$$

where

$$T_n(\eta) = \cos(n \cos^{-1}(\eta)) \tag{2.18}$$

Fundamental sinuous   Subharmonic sinuous

Fundamental varicose   Subharmonic varicose
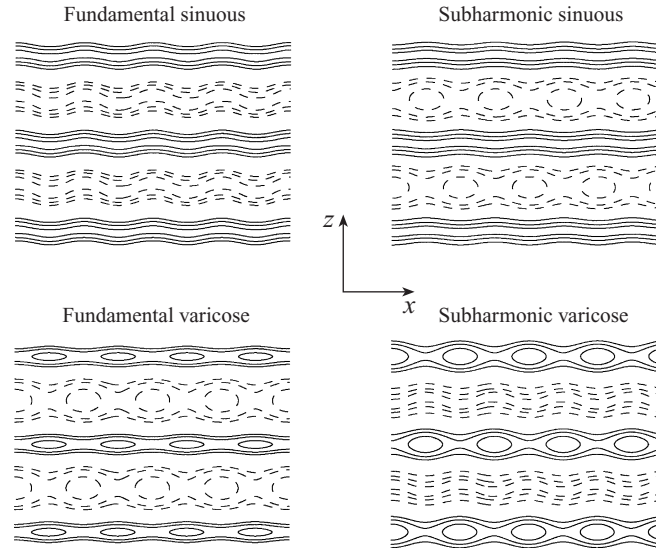

FIGURE 2. Sketch of streak instability modes in the (x, z)-plane over four streamwise and two spanwise periods, by contours of the streamwise velocity. The low-speed streaks are drawn with solid lines while dashed lines are used for the high-speed streaks.

is the Chebyshev polynomial of degree n defined in the interval $-1 \leqslant \eta \leqslant 1$. We use

$$\eta_j = \cos \frac{\pi j}{N}, \quad j = 0, 1, \ldots, N,$$

as collocation points, that is, the extrema of the Nth-order Chebyshev polynomial T_N plus the endpoints of the interval.

The calculations are performed using 121 ($N = 120$) Chebyshev collocation points in y, and with the Fourier series in z truncated after fifteen modes. The wall-normal domain varies in the range $(0, y_{max})$, with y_{max} well outside the boundary layer (typically y_{max} is taken equal to 50). The Chebyshev interval $-1 \leqslant \eta \leqslant 1$ is transformed to the computational domain $0 \leqslant y \leqslant y_{max}$ by the use of the conformal mapping

$$y = a \frac{1 + \eta}{b - \eta}, \tag{2.19}$$

where

$$a = \frac{y_i \, y_{max}}{y_{max} - 2y_i} \quad \text{and} \quad b = 1 + \frac{2a}{y_{max}}.$$

This mapping puts half the grid points in the region $0 \leqslant y \leqslant y_i$, with y_i chosen to be equal to 8.

The unknown functions $\hat{p}_k = \hat{p}_k(y)$ may now be approximated by

$$\hat{p}_k^N(y) = \sum_{n=0}^{N} \bar{p}_k^n \tilde{T}_n(y),$$

where $\tilde{T}_n(y) = T_n(\eta)$ with $\eta \mapsto y$ being the mapping (2.19). The Chebyshev coefficients $\bar{p}_k^n$, $n = 0, \ldots, N$, are determined by requiring equation (2.12) to hold for $\hat{p}_k^N$ at the collocation points y_j, $j = 1, \ldots, N - 1$. The boundary conditions (2.13) are enforced

by adding the equations

$$\sum_{n=0}^{N} \bar{p}_k^n \tilde{T}_{n,y}(0) = \sum_{n=0}^{N} \bar{p}_k^n \tilde{T}_{n,y}(y_{\max}) = 0,$$

where subscript n, y denotes the y-derivative of the nth Chebyshev polynomial.

2.3. *Chebyshev polynomials in complex space*

The discretization leads to a generalized eigenproblem with the two matrices containing only real elements; hence, the solutions will consist of either real eigenvalues or complex conjugate pairs. No strictly damped solutions can be found using these equations together with an integration path running along the real y-axis from 0 to $y_{\max}$, since the neglect of viscosity introduces a continuous spectrum of singular neutral modes. Lin (1944) performed an asymptotic analysis on the Orr–Sommerfeld equation, requiring the inviscid eigenvalue problem (the Rayleigh equation) to be a limit of the viscous one when the Reynolds number approaches infinity. For this to apply, he found that the integration path in the inviscid case could be taken on the real axis if $c_i > 0$ and that it should be taken in the complex plane for $c_i \leqslant 0$, in such a way that the singularities lie on the same side of the integration path as in the $c_i > 0$ case.

Information on the singularities is contained in the system's determinant. We are satisfied here with the approximate location of the singularities and to simplify the analysis the mean field with the shape assumption is considered, i.e.

$$U(y, z) = U_B(y) + \frac{A_s}{2} u_s(y; \beta) e^{i\beta z} + \frac{A_s}{2} u_s(y; \beta) e^{-i\beta z}, \tag{2.20}$$

with U_B the Blasius solution, u_s the streak mode shape provided by the analysis of Andersson *et al.* (1999*a*) and scaled so that $\max[u_s(y; \beta)] = 1$, A_s the amplitude of the streak and β the spanwise wavenumber. Figure 1 shows the streak mode shape u_s. Introducing expansion (2.20) into equation (2.12) yields an equation that holds for each integer k:

$$\frac{A_s}{2} u_s \left(\frac{\partial^2}{\partial y^2} - \beta^2 (k - 1 + \gamma)(k - 3 + \gamma) - \alpha^2 \right) \hat{p}_{k-1} - A_s u_{s,y} \frac{\partial}{\partial y} \hat{p}_{k-1}$$

$$+ (U_B - c) \left(\frac{\partial^2}{\partial y^2} - \beta^2 (k + \gamma)^2 - \alpha^2 \right) \hat{p}_k - 2U_{B,y} \frac{\partial}{\partial y} \hat{p}_k$$

$$+ \frac{A_s}{2} u_s \left(\frac{\partial^2}{\partial y^2} - \beta^2 (k + 1 + \gamma)(k + 3 + \gamma) - \alpha^2 \right) \hat{p}_{k+1} - A_s u_{s,y} \frac{\partial}{\partial y} \hat{p}_{k+1} = 0, \tag{2.21}$$

plus boundary conditions (2.13).

By rewriting equations (2.21) and (2.13) as a system of first-order equations and studying the system's determinant, the singularities can be identified analytically as the roots of the equation

$$\prod_{k=1}^{K} \left\{ U_B - c + A_s u_s \cos \left(\frac{k\pi}{K+1} \right) \right\} = 0,$$

where K is the number of Fourier modes. For small values of c_i the approximate location of each singularity in the complex y-plane can be identified with a Taylor
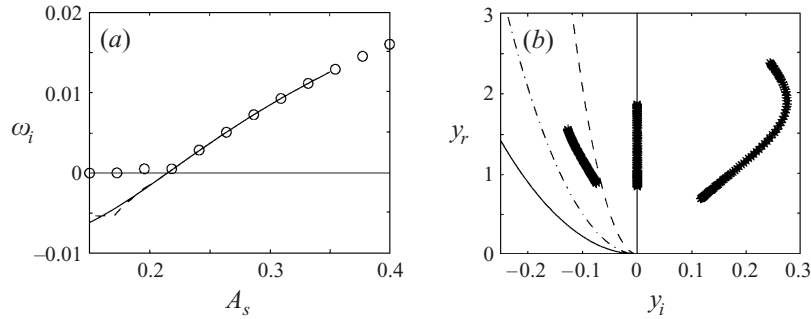
FIGURE 3. (*a*) Temporal growth rate of the fundamental varicose mode versus the streak amplitude for $\alpha = 0.2$ and $\beta = 0.45$ (O, real integration path; - - -, complex integration path with $B = 0.01$; ——, complex integration path with $B = 0.03$). (*b*) The three curved lines denote different integration paths: - - -, $B = 0.01$; -----, $B = 0.02$; ——, $B = 0.03$. The thick segments of stars denote the singular segments for three different streak amplitudes. From the left: $A_s = 0.15$ (amplified modes do not exist), 0.215 (the least stable discrete mode is neutral) and 0.35 (at least one amplified mode exists). Only for the last case is the real integration path suitable.

expansion around $y = y_r$, i.e.

$$U_B(y_r) + A_s u_s(y_r; \beta) \cos\left(\frac{k\pi}{K+1}\right) = c_r + \text{h.o.t.}$$

and to first order these locations are

$$y_s = y_r + \mathrm{i}\frac{c_i}{U_{B,y}(y_r) + A_s u_{s,y}(y_r)\cos\left(k\pi/(K+1)\right)}. \tag{2.22}$$

These are, as might have been expected, the values of y for which the base flow velocity becomes equal to c at the discrete values of the z-coordinate imposed by the truncated Fourier expansion in z. Clearly, y_s crosses the real y-axis when c_i changes sign, so that the integration path has to go out into the complex y-plane in order for the singularities to lie on the same side of the path. Integration in the complex plane is necessary when neutral curves are sought. The mapping

$$y^c = y - \mathrm{i}B(y_{\max}\, y - y^2)^{1/2} \tag{2.23}$$

allows the computation of damped (and neutral) modes. It is introduced into (2.19), that is $y^c \mapsto \eta^c$, to deliver a curve in the complex plane with endpoints in $\eta^c = -1$ and 1. Complex Chebyshev polynomials $T_n^c(\eta^c)$ are defined by using (2.18), and the unknown functions are approximated using this new basis. This can be done since the analytic continuation of a polynomial is given by the same polynomial but with a complex argument.

As can be inferred from equation (2.22) the singularities corresponding to a given set of problem parameters are confined to a finite segment in the complex y-plane. For amplified modes this segment is found in the right half-plane in figure 3(*b*); for damped modes it is displaced to the left half-plane, whereas for neutral modes the singular segment is a subset of the real axis. In figure 3(*a*) the results of three calculations of the temporal growth rate are plotted versus the streak amplitude, employing the shape assumption for given streamwise, $\alpha = 0.2$, and spanwise, $\beta = 0.45$, wavenumbers. The circles are obtained by integrating over the real y-axis; as the amplitude A_s of the streak decreases, so does the largest growth rate of the instability ω_i, until the value
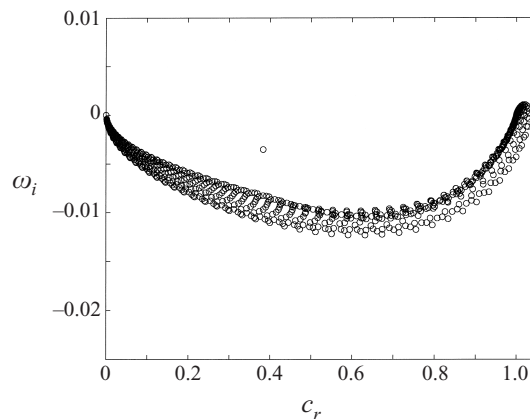
FIGURE 4. Eigenvalue spectrum of the fundamental varicose mode for $\alpha = 0.2$, $\beta = 0.45$ and $A_s = 0.18$, displayed as temporal growth rate versus phase speed. It is obtained using a complex integration path with $B = 0.03$.

$A_s \approx 0.215$ below which only quasi-neutral modes are found. For such modes the real integration path is located on the wrong side of the singularities. If the complex integration path denoted by a dashed line in both figures (corresponding to $B = 0.01$ in the mapping (2.23)) is employed, the integration correctly follows the damped mode down to an amplitude of about 18%. Clearly one can proceed to even smaller amplitudes simply by increasing B, i.e. by displacing the integration contour further into the negative y_i region. For example, the dotted-dashed contour in figure 3(b) can be used, or the continuous line path (corresponding to $B = 0.03$). The latter integration path has been used and the resulting full spectrum is shown in figure 4 for a streak amplitude of 0.18. The continuous spectrum of singular neutral modes is displaced downward and an isolated, damped mode can be identified at a phase speed close to 0.4. Provided that the singular segment lies on the correct side of the integration path, changes in the path do not affect this eigenvalue; the continuous spectrum is, instead, further moved towards lower values of ω_i for increasing B. Values of B between 0.01 and 0.03 have been used in most of the calculations identifying neutral modes in the present paper.

Clearly other integration paths are also possible; in fact, any complex detour that leaves the singularities to its right side in the complex y-plane will yield the correct physical eigenvalues. Since the physical solutions vanish rapidly at infinity there is no need for the integration path to return to the real axis at $y = y_{max}$ in order to enforce the boundary conditions at the free stream (Peter Schmid, private communication). In some calculations, the mapping

$$y^c = y - iD(2y_{max} y - y^2)^{1/2} \qquad (2.24)$$

corresponding to a quarter of an ellipse has also been used successfully (D was taken equal to 0.006 in our calculations).

The growing and decaying solutions obtained by our procedure are the asymptotic limits of amplified and damped modes of the viscous stability equations as the Reynolds number approaches infinity (Lin 1955). We re-emphasize here that it is only by the use of this procedure that neutral (and damped) modes can be defined without ambiguities.

2.4. *DNS method*

2.4.1. *Numerical scheme*

The simulation code (see Lundbladh *et al.* 1999) employed for the present computations uses spectral methods to solve the three-dimensional, time-dependent, incompressible Navier–Stokes equations. The algorithm is similar to that of Kim, Moin & Moser (1987), i.e. Fourier representation in the streamwise and spanwise directions and Chebyshev polynomials in the wall-normal direction, together with a pseudo-spectral treatment of the nonlinear terms. The time advancement used is a four-step low-storage third-order Runge–Kutta method for the nonlinear terms and a second-order Crank–Nicolson method for the linear terms. Aliasing errors from the evaluation of the nonlinear terms are removed by the $\frac{3}{2}$-rule when the FFTs are calculated in the wall-parallel plane. In the wall-normal direction it has been found more efficient to increase the resolution rather than using dealiasing.

To correctly account for the downstream boundary layer growth a spatial technique is necessary. This requirement is combined with the periodic boundary condition in the streamwise direction by the implementation of a 'fringe region', similar to that described by Bertolotti, Herbert & Spalart (1992). In this region, at the downstream end of the computational box, the function $\lambda(x)$ in equation (2.25) is smoothly raised from zero and the flow is forced to a desired solution v in the following manner:

$$\frac{\partial \boldsymbol{u}}{\partial t} = NS(\boldsymbol{u}) + \lambda(x)(\boldsymbol{v} - \boldsymbol{u}) + \boldsymbol{g}, \tag{2.25}$$

$$\nabla \cdot \boldsymbol{u} = 0, \tag{2.26}$$

where $\boldsymbol{u}$ is the solution vector and $NS(\boldsymbol{u})$ the right-hand side of the (unforced) momentum equations. Both $\boldsymbol{g}$, which is a disturbance forcing, and $\boldsymbol{v}$ may depend on the three spatial coordinates and time. The forcing vector $\boldsymbol{v}$ is smoothly changed from the laminar boundary layer profile at the beginning of the fringe region to the prescribed inflow velocity vector. This is normally a boundary layer profile, but can also contain a disturbance. A convenient form of the fringe function is as follows:

$$\lambda(x) = \lambda_{\max} \left[S\left(\frac{x - x_{\text{start}}}{\Delta_{\text{rise}}}\right) - S\left(\frac{x - x_{\text{end}}}{\Delta_{\text{fall}}} + 1\right) \right], \tag{2.27}$$

where $\lambda_{\max}$ is the maximum strength of the damping, x_{start} to x_{end} the spatial extent of the region where the damping function is non-zero and Δ_{rise} and Δ_{fall} parameters which specify the 'rise' and 'fall' distance of the damping function. $S(a)$ is a smooth step function rising from zero for negative a to one for $a \geqslant 1$. We have used the following form for S, which has the advantage of having continuous derivatives of all orders:

$$S(a) = \begin{cases} 0, & a \leqslant 0 \\ 1 \Big/ \left[1 + \exp\left(\dfrac{1}{a-1} + \dfrac{1}{a}\right)\right], & 0 < a < 1 \\ 1, & a \geqslant 1. \end{cases} \tag{2.28}$$

This method damps disturbances flowing out of the physical region and smoothly transforms the flow to the desired inflow state, with a minimal upstream influence.

In order to set the free-stream boundary condition not too far from the wall, a generalization of the boundary condition used by Malik, Zang & Hussaini (1985) is implemented. Since it is applied in Fourier space with different coefficients for each

wavenumber, it is non-local in physical space and takes the following form:

$$\frac{\partial \hat{\boldsymbol{u}}}{\partial y} + |k|\hat{\boldsymbol{u}} = \frac{\partial \hat{\boldsymbol{v}}_0}{\partial y} + |k|\hat{\boldsymbol{v}}_0, \tag{2.29}$$

where k is the absolute value of the horizontal wavenumber vector and $\hat{\boldsymbol{u}}$ is the Fourier transform of $\boldsymbol{u}$. Here $\boldsymbol{v}_0$ denotes the local solution of the Blasius equation and $\hat{\boldsymbol{v}}_0$ its Fourier transform.

2.4.2. *Disturbance generation and parameter setting*

The numerical implementation provides several possibilities for disturbance generation. The complete velocity vector field from the linear results by Andersson *et al.* (1999*a*) is used for the primary disturbance. These optimally growing streaks, here denoted $\boldsymbol{v}_{\mathrm{d}}$, are introduced in the fringe region by adding them to the Blasius solution to yield the forcing vector $\boldsymbol{v} = \boldsymbol{v}_0 + \boldsymbol{v}_{\mathrm{d}}$.

In order to trigger a secondary instability of the streaks a harmonic localized wall-normal volume force is added. The harmonic forcing, $\boldsymbol{g} = (0, F, 0)$, is constructed as an exponentially (in space) decaying function centred at $y = y_0$ and $x = x_{\mathrm{loc}}$:

$$F = C \exp\left[-((x - x_{\mathrm{loc}})/x_{\mathrm{scale}})^2\right] \exp\left[-((y - y_0)/y_{\mathrm{scale}})^2\right] g(z) f(t), \tag{2.30}$$

where the constant C determines the strength of the forcing and the parameters x_{scale} and y_{scale} its spatial extent. The time dependence is provided by the function

$$f(t) = S(t/t_{\mathrm{scale}}) \cos(\omega t), \tag{2.31}$$

where ω is the angular frequency and the function S has been used again in $f(t)$ to ensure a smooth turn on of the forcing (of duration t_{scale}) in order to avoid problems with transients that may grow and cause transition in the flow. It is also possible to choose the spanwise symmetry of the forcing, to separately excite two classes of secondary disturbances; in

$$g(z) = \cos(\beta z + \phi), \tag{2.32}$$

we choose $\phi = 0$ or $\pi/2$ for varicose or sinuous symmetries, respectively.

The box sizes and resolutions used for the simulations presented in this paper are displayed in table 1. The dimensions of the boxes are reported in multiples of δ_0, which here denotes the Blasius thickness at the beginning of the computational box. Box 1 is used to produce the nonlinear streaks and study their secondary instability, while Box 2 is employed to verify the scaling property introduced in § 3.2; Box 3, Box 4 and Box 5 are, instead, used to test the DNS against the linear results (see figure 7*a*). The Reynolds numbers based on δ_0 are also reported in the table. For the calculations presented on the secondary instability induced by harmonic forcing, we use $x_{\mathrm{loc}} = 300\delta_0$ from the beginning of the computational box, and $y_0 = 3\delta_0$ with x_{scale} and y_{scale} of $35\delta_0$ and $3\delta_0$, respectively.

3. DNS results

3.1. *Nonlinear development of the streaks*

Nonlinear mean fields are computed solving the full Navier–Stokes equations in a spatially evolving boundary layer, using the optimal streaks as initial conditions. The complete velocity vector field from the linear results by Andersson *et al.* (1999*a*) is used as input close to the leading edge and the downstream nonlinear development is monitored for different initial amplitudes of the perturbation. This is shown in

$xl \times yl \times zl$ δ_0	$nx \times ny \times nz$ (resolution)	Re_{δ_0}
Box 1	$1940 \times 34.4 \times 22.06$	$576 \times 65 \times 32$	272.2
Box 2	$1940 \times 34.4 \times 22.06$	$576 \times 65 \times 32$	332.1
Box 3	$1702 \times 34.4 \times 16.68$	$512 \times 81 \times 8$	264.6
Box 4	$3096 \times 34.4 \times 16.68$	$1024 \times 81 \times 8$	591.6
Box 5	$3404 \times 34.4 \times 14.71$	$1024 \times 81 \times 8$	948.7

TABLE 1. Resolution and box dimensions for the simulations presented. The box dimensions include the fringe region, and are made dimensionless with respect to δ_0, the Blasius length scale at the beginning of the computational box. The parameters zl and nz represent the full span and the total number of Fourier modes, respectively. Note that zl corresponds in all cases to one spanwise wavelength of the primary disturbance.
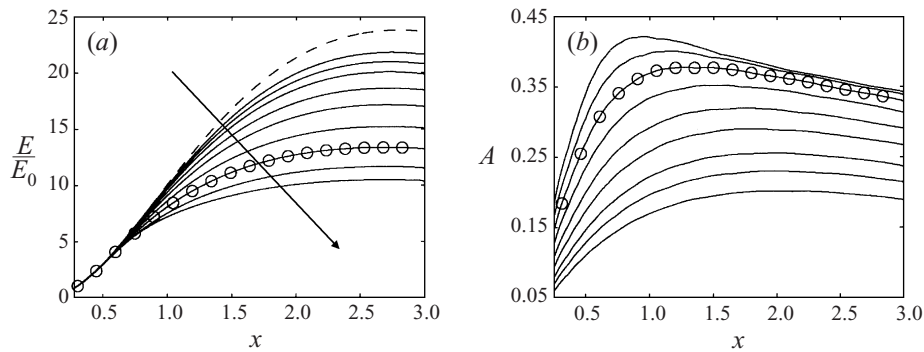
FIGURE 5. (a) The energy of the primary disturbance, E, normalized with its initial value, E_0, versus the streamwise coordinate, x, for $\beta = 0.45$ and $Re_\delta = 430$. Here x has been made non-dimensional using the distance L to the leading edge. The arrow points in the direction of increasing initial energies, $E_0 = 2.92 \times 10^{-2}, 3.97 \times 10^{-2}, 5.18 \times 10^{-2}, 7.30 \times 10^{-2}, 9.78 \times 10^{-2}, 1.36 \times 10^{-1}, 1.81 \times 10^{-1}, 2.33 \times 10^{-1}, 2.91 \times 10^{-1}$ (E_0 is computed at $x = 0.3$). The dashed line represents the optimal linear growth. (b) The downstream amplitude development for the same initial conditions as in (a). The amplitude A is defined by equation (3.2). (The two lines have been circled for future reference.)

figure 5(a), where all energies are normalized by their initial values. The dashed line corresponds to an initial energy small enough for the disturbance to obey the linearized equations. For this case the maximum of the energy is obtained at $x = 2.7$; note that this location of maximum energy is weakly dependent on the initial amplitude, even for quite large values of the initial energy.

A contour plot in the (z, y)-plane of the nonlinear mean field corresponding to the circled line in figure 5(a) at $x = 2$ is shown in figure 6(b). This velocity field may be expanded in the sum of cosines

$$U(y, z) = \sum_{k=0}^{\infty} U_k(y) \cos(k\beta z) \tag{3.1}$$

where U_0 differs from the Blasius solution U_B by the mean flow distortion term. To be able to quantify the size of the primary disturbance field an amplitude A is defined as

$$A = \tfrac{1}{2}[\max_{y,z}(U - U_B) - \min_{y,z}(U - U_B)]. \tag{3.2}$$

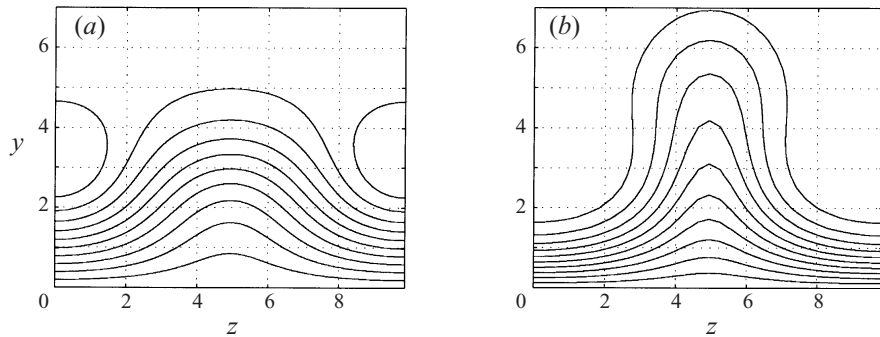When the shape assumption is adopted, A coincides with A_s. Figure 5(b) displays

FIGURE 6. (a) Contour plot in a (z, y)-plane of the primary disturbance streamwise velocity using the shape assumption. The spanwise wavenumber is $\beta = 0.45$, the streamwise position $x = 2$ and the amplitude $A_s = 0.36$. (b) Contour plot in a (z, y)-plane of the nonlinear mean field corresponding to the circled line in figure 5(a) at $x = 2$ (where $A = 0.36$). Here $Re_\delta = 430$. In both figures the coordinates y and z have been made non-dimensional using the local Blasius length scale δ, at the streamwise position $x = 2$. In fact, for all y, z plots hereafter the cross-stream coordinates have been scaled using the local Blasius length scale.

the downstream amplitude development for the same initial conditions as figure 5(a). Notice that the amplitude reaches its maximum value upstream of the position where the energy attains its peak, and starts to decrease at a position where the energy is still increasing. This is due to the thickening of the boundary layer.

The effect of the nonlinear interactions on the base flow are shown by the contour plots in figure 6. Figure 6(a) displays the primary disturbance obtained using the shape assumption with $A_s = 0.36$, while 6(b) shows a fully nonlinear mean field, characterized by the same disturbance amplitude. In the latter case, the low-speed region is narrower, therefore associated with higher spanwise gradients, and displaced further away from the wall.

A base flow like the one presented in figure 6(b) is representative of flat-plate boundary layer flows dominated by streamwise streaks as encountered in experiments (Bakchinov *et al.* 1995; Westin *et al.* 1994; Kendall 1985, 1990) and simulations (Berlin & Henningson 1999).

3.2. *Scaling of the mean field*

In Andersson *et al.* (1999a) a scaling property of the optimal streamwise streaks in the flat-plate boundary layer was found to exist. In a linearized setting, they considered an upstream velocity perturbation at the leading edge of the flat plate, $\boldsymbol{u}_{\text{in}}(0)$, and its downstream response, $\boldsymbol{u}_{\text{out}}(x)$, a distance x from the leading edge, and maximized the output energy $E(\boldsymbol{u}_{\text{out}}(x)) = E(x, \beta, E_0, Re)$ over all initial disturbances with fixed energy $E(\boldsymbol{u}_{\text{in}}(0)) = E_0$.

The disturbance energy can be written

$$E(\boldsymbol{u}(x)) = \int_0^{2\pi/\beta} \int_0^\infty \left(u^2 + \frac{\bar{v}^2}{Re} + \frac{\bar{w}^2}{Re} \right) \, \mathrm{d}y \, \mathrm{d}z, \tag{3.3}$$

where $\bar{v} = v\sqrt{Re}$ and $\bar{w} = w\sqrt{Re}$ are the cross-stream velocities in boundary layer scales. The optimal disturbances, which were calculated using the linearized, steady boundary layer approximation, were found to consist of streamwise vortices developing into streamwise streaks. Since streamwise aligned vortices contain no streamwise
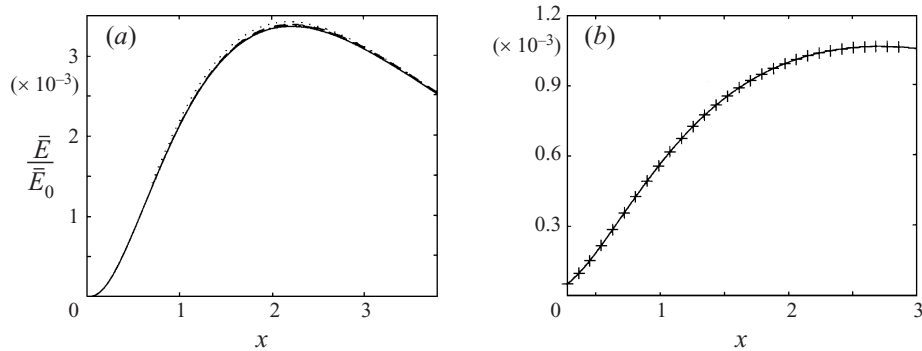
FIGURE 7. The spatial energy growth versus the streamwise coordinate, for the spanwise wavenumber, $\beta = 0.45$. (*a*) With three small-amplitude solutions to the Navier–Stokes equations for Reynolds numbers (- - -, $Re = 1 \times 10^6$; ----, $Re = 5 \times 10^5$; $\cdots$, $Re = 1 \times 10^5$), and (——) one Reynolds number independent solution from the linearized, steady boundary layer approximations. (*b*) With an initial amplitude large enough to induce considerable nonlinear effects, $A = 0.30$. Here the two curves represent solutions to the Navier–Stokes equations for two different Reynolds numbers (——, $Re = 5 \times 10^5$; +, $Re = 7.5 \times 10^5$).

velocity component, the energy at the leading edge E_0 can be written as

$$E_0 = \frac{\bar{E}_0}{Re}, \quad \text{where} \quad \bar{E}_0 = \int_0^{2\pi/\beta} \int_0^\infty (\bar{v}^2 + \bar{w}^2) \, dy \, dz, \tag{3.4}$$

with $\bar{E}_0$ independent of the Reynolds number. The boundary layer equations governing $(u, \bar{v}, \bar{w}, \bar{p})$, here $\bar{p} = pRe$, contain no explicit dependence on the Reynolds number; furthermore, all velocities are $O(1)$ a distance sufficiently far downstream of the plate leading edge. Hence, the streamwise velocity component will dominate in the disturbance energy (3.3) and the output energy obeys the scaling law

$$\bar{E}(x, \beta, \bar{E}_0) = \lim_{Re \to \infty} E(x, \beta, \bar{E}_0, Re). \tag{3.5}$$

This scaling property holds also when the solutions are obtained from the Navier–Stokes equations, if $u = 0$ at $x = 0$. In figure 7 both linear and nonlinear solutions obtained from the Navier–Stokes equations are presented which verify (3.5).

Figure 7(*a*) displays $\bar{E}/\bar{E}_0$ versus x for the spanwise wavenumber, $\beta = 0.45$. The solid line corresponds to a solution obtained using the linearized, steady boundary layer approximation. The other three lines represent results obtained from solving the Navier–Stokes equations, for three different Reynolds numbers, with initial disturbance energies small enough to yield a linear evolution. Figure 7(*a*) shows that the boundary layer approximation is valid and yields solutions in agreement with those obtained from the Navier–Stokes simulations.

Figure 7(*b*) depicts two curves representing the spatial development of $\bar{E}$ using an initial energy, $\bar{E}_0$, large enough to induce substantial nonlinear effects. The two curves, which represent solutions to the Navier–Stokes equations for the same initial energy and spanwise wavenumber, collapse onto one, although they correspond to two different Reynolds numbers. From figure 7(*b*) we conclude that the scaling property (3.5) holds also when the velocity field of the primary disturbance is fully nonlinear.

To clarify the implication of (3.5), consider the same dimensional problem with the dimensional energy denoted E^* scaled with two different length scales, L and L_1.

We write

$$E^*(x, \beta, \bar{E}_0, Re) = E^*(x^1, \beta^1, \bar{E}_0^1, Re^1), \tag{3.6}$$

where the variables are scaled as

$$x^* = xL = x^1 L_1, \quad \beta^* = \beta\sqrt{\frac{U_\infty}{vL}} = \beta^1\sqrt{\frac{U_\infty}{vL_1}}, \quad Re = \frac{U_\infty L}{v}, \quad Re_1 = \frac{U_\infty L_1}{v}; \tag{3.7}$$

here x^* and β^* are the dimensional downstream position and spanwise wavenumber, respectively. The disturbance energies scale as

$$E^* = E U_\infty^2 \delta^2 = E^1 U_\infty^2 \delta_1^2 \quad \text{and} \quad \bar{E}_0 = \bar{E}_0^1. \tag{3.8}$$

Introducing $c^2 = L/L_1 = \delta^2/\delta_1^2$ and rewriting the right-hand expression in (3.6), in the variables x, β, Re we obtain

$$c^2 E(x, \beta, \bar{E}_0, Re) = E(c^2 x, \beta/c, \bar{E}_0, Re/c^2). \tag{3.9}$$

Now letting the Reynolds numbers tend to infinity and using (3.5) we get

$$c^2 \bar{E}(x, \beta, \bar{E}_0) = \bar{E}(c^2 x, \beta/c, \bar{E}_0), \tag{3.10}$$

for each $c > 0$.

An important physical implication of (3.5) can now be inferred from relation (3.10). Since (3.10) is Reynolds number independent, a non-dimensional solution $\bar{E}(x, \beta, \bar{E}_0)$ represent a continuous set of physical solutions in (x^*, β^*)-space, for a fixed $\bar{E}_0$. We have seen that an initial array of streamwise aligned vortices at the leading edge will result in an array of streamwise streaks downstream. Since the streamwise and spanwise length scales are coupled, increasing the spanwise length scale at the leading edge will yield the same downstream behaviour of the solutions but on a larger streamwise length scale.

In figure 8 the curve $(c^2 x, \beta/c)$, with $x = 2$ and $\beta = 0.45$, is shown. From (3.10) the results along this curve are known and correspond to a rescaling of the solutions calculated at $x = 2$ and $\beta = 0.45$ (represented by the star in figure 8).

Note that (3.10) implies that $\bar{E}$ increases linearly as the streamwise coordinate x increases, and the spanwise wavenumber β decreases (cf. figure 8). The increase in the energy of the streak E^* is a result of the widening of the cross-stream spatial extent of the disturbance. Since the shape of the streak velocity profile is the same, this implies that the amplitude remains constant along the curve $x\beta^2 = \text{constant}$. In contrast, the energy of the corresponding initial vortex E_0^* remains the same for this parameter combination. This implies that the amplitude of the initial vortex, A_v, increases linearly with the spanwise wavenumber, i.e. $A_v \sim \beta$. Thus the amplitude of the initial vortex needed to produce a fixed amplitude of the streak along the curve $x\beta^2 = \text{constant}$ decreases in a manner inversely proportional to the spanwise wavelength.

3.3. *Secondary instability results from DNS*

In this section direct numerical simulations of the secondary instability of streaks in a spatially growing flat-plate boundary layer are compared to the results from the inviscid secondary instability theory. This is done to ensure that the inviscid approximation is appropriate and can be used in further investigations and parametric studies of streak instabilities.

The spatial stability problem is defined by the use of a real frequency ω and a complex wavenumber $\alpha = \alpha_r + i\alpha_i$. Here the spatial growth rate $-\alpha_i$ is obtained by
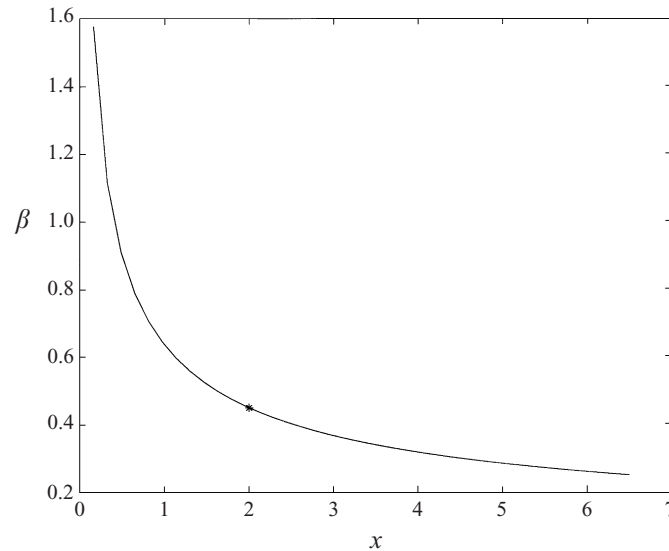
FIGURE 8. Loci of spanwise wavenumbers, β, and streamwise positions, x, representing the known solutions from the linear or nonlinear calculations at $x = 2$ with $\beta = 0.45$. The streamwise position and the spanwise wavenumber have been made non-dimensional using the distance from the leading edge L and the Blasius length scale $\delta = (Lv/U_\infty)^{1/2}$, respectively.

monitoring the maximum of the streamwise velocity component of the secondary disturbance. The secondary disturbances are triggered using the harmonic forcing introduced in §2.4.2, allowing the two symmetries of fundamental type which can be excited separately. The amplitude of the volume force is selected low enough to yield linear secondary disturbances, avoiding the appearance of higher harmonics in the frequency spectra.

To choose the forcing frequency for the DNS, temporal linear secondary stability calculations for the sinuous mode are performed using the nonlinear mean field corresponding to the circled line in figure 5(a), at the local position $x = 2$. The selected mean field has amplitude $A = 0.36$, close to the threshold value for secondary instability in plane channel flow (Elofsson *et al.* 1999). The maximum temporal growth is found for $\alpha = 0.257$, corresponding to a secondary disturbance frequency of 0.211.

The direct numerical simulations for the fundamental sinuous mode of the secondary instability are carried out using this forcing frequency, $\omega = 0.211$, and the velocity fields are Fourier transformed in time to obtain the amplitude variation in the streamwise direction and the cross-stream distribution of the disturbance velocity at the frequency of the forcing.

Figure 9(a) shows the u_{rms} distribution of the fundamental sinuous mode at $x = 2$. Note how the disturbance fluctuations follow quite closely the dashed line representing the contour of constant value of the mean field velocity corresponding to the phase speed of the secondary instability, $U = c_r = 0.80$. The solid line in figure 9(b) represents the spatial growth rate of the sinuous mode obtained from the direct numerical simulations. Here the secondary instability is excited at the streamwise position $x = 0.85$. However, since the local forcing does not input pure eigenmodes the values of the growth rates are measured from an x-position downstream of the forcing, where the onset of an 'eigenfunction' is identified.

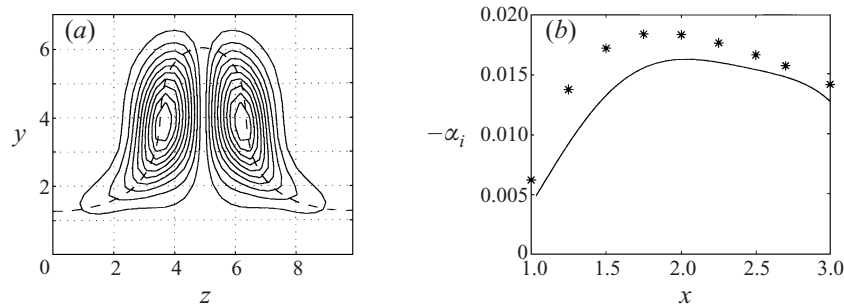Linear temporal stability calculations, using the real part of the streamwise

FIGURE 9. (a) Isocontours of r.m.s. values of the streamwise velocity component of the secondary disturbance ($\omega_r = 0.211$) for the fundamental sinuous mode at $x = 2$, obtained from the DNS. The dashed line represents the contour of the constant value of the mean field corresponding to the phase speed of the disturbance ($U = c_r = 0.80$). (b) Spatial growth rates, α_i versus x; ——, DNS data with $Re_\delta = 430$ and $\beta = 0.45$; *, linear temporal inviscid stability calculations using mean fields at each corresponding x-position and streamwise wavenumber $\alpha_r = 0.260$.

wavenumber obtained from the direct numerical simulations, $\alpha_r = 0.260$, are also performed, employing mean fields extracted at different streamwise positions from the DNS. In order to compare the spatial results to the growth rates obtained from the temporal inviscid stability problem (2.12), (2.13) a transformation first proposed by Gaster (1962) is employed:

$$\omega_i = -\frac{\alpha_i}{\partial\alpha/\partial\omega}. \tag{3.11}$$

From the temporal eigenvalues, Gaster's transformation (3.11) provides estimates of spatial growth rates (cf. the stars in figure 9b). The agreement between the stability theory and the full simulation results can be regarded as good, since the linear stability calculations are inviscid and performed under the assumptions of parallel mean flow. Note that, as one could expect, the inviscid approximation provides a slight overestimate of the amplification factors, and that closer agreement is found as the Reynolds number increases; here $Re = 500\,000$ at the streamwise position $x = 2.7$.

Using the same saturated mean field, direct numerical simulations are also carried out for the fundamental varicose mode of the secondary instability. Attempts to identify instabilities are made with different frequencies and for different streamwise and wall-normal positions of the forcing in the direct simulations. Also, linear stability calculations at $x = 2$ and for a range of different streamwise wavenumbers are performed. Both methods produce only stable solutions for this symmetry of the disturbances.

However, linear calculations using as base flow the streaks obtained with the largest initial energy tested (see figure 5), produce small positive temporal growth rates for the fundamental varicose instability. We then proceed as for the sinuous case: the largest growth rate, ω_i, is identified to correspond, at $x = 2$, to a streamwise wavenumber $\alpha = 0.250$ and a frequency $\omega_r = 0.217$. This value is used in the DNS forcing and the spatial growth rates obtained are compared to linear stability calculations performed at different streamwise positions for $\alpha_r = 0.252$. The results are shown in figure 10(b); the inviscid analysis gives small positive growth rates, while in the DNS the perturbation growth rates remain close to neutral as x exceeds 2.

Figure 10(a) shows the u_{rms} distribution of the fundamental varicose mode together with the contour of constant value of the mean field velocity corresponding to the phase speed of the secondary instability, i.e. $U = c_r = 0.863$. Note also here the close
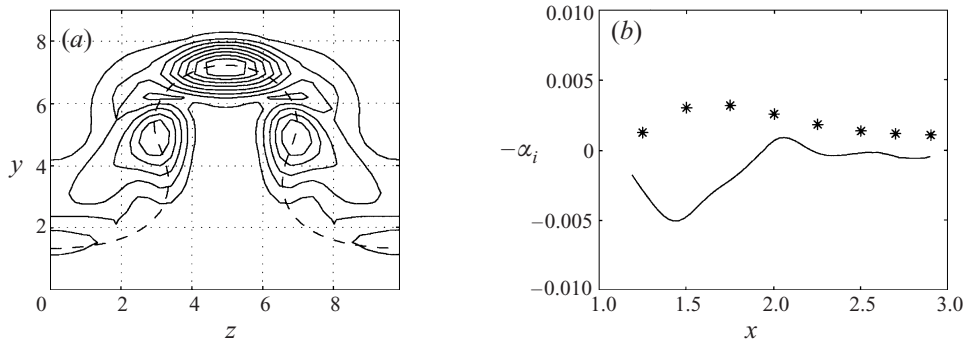
FIGURE 10. (*a*) Isocontours of r.m.s. values of the streamwise velocity component of the secondary disturbance ($\omega_r = 0.217$) for the fundamental varicose mode at $x = 2$, obtained from the DNS. The dashed line represents the contour of the constant value of the mean field corresponding to the phase speed of the disturbance ($U = c_r = 0.863$). (*b*) Spatial growth rates α_i versus x; ——, DNS data with $Re_\delta = 430$ and $\beta = 0.45$; $*$, linear temporal inviscid stability calculations using mean fields at each corresponding x-position and streamwise wavenumber $\alpha_r = 0.252$.

correspondence between the critical layer (displayed in the figure with a dashed line) and regions of intense u-fluctuations.

From the above calculations and comparisons we draw as first conclusion that the secondary instability of streamwise streaks is initially of sinuous type, and that the essential stability features can successfully be captured by an inviscid approach. The above statements are further confirmed by the results described below.

4. Inviscid secondary instability results

4.1. *The shape assumption versus the nonlinearly developed mean field*

As a preliminary investigation, the secondary instability of streaks approximated by the shape assumption was parametrically studied (Andersson *et al.* 1999*b*). Comparison of the results with those obtained from calculations where the base flow is the nonlinearly developed streak demonstrate the inapplicability of the shape assumption for this type of study (except for sinuous symmetries where a qualitative agreement can still be claimed).

In figures 11 and 12 the u-eigenfunctions, obtained with the shape assumption approximation and the nonlinear mean field, respectively, are displayed for the parameters indicated.

Figure 11(*a*) shows the fundamental sinuous mode which is characterized by out-of-phase oscillations on either side of the low-speed streak, whereas the near-wall region is relatively quiescent. The subharmonic sinuous mode (figure 11*b*) has real and imaginary parts of u symmetric around the $z = 0$ and $z = 2\pi/\beta$ axes. This eigenfunction shows a striking resemblance to that obtained by Ustinov (1998) who solved the linearized Navier–Stokes equations in time; it is also the same high-frequency mode triggered in the experiments by Bakchinov *et al.* (1995). In figure 11(*c*) the fundamental varicose mode is displayed. In-phase fluctuations are spread in a z-range around π/β and halfway through the undisturbed boundary layer height. Some effect is also noticeable around $z = 0$ and $2\pi/\beta$, close to the wall. This mode is also very similar to that computed by Ustinov (1998). The subharmonic varicose mode (figure 11*d*) is characterized by almost the same phase speed as that of its fundamental
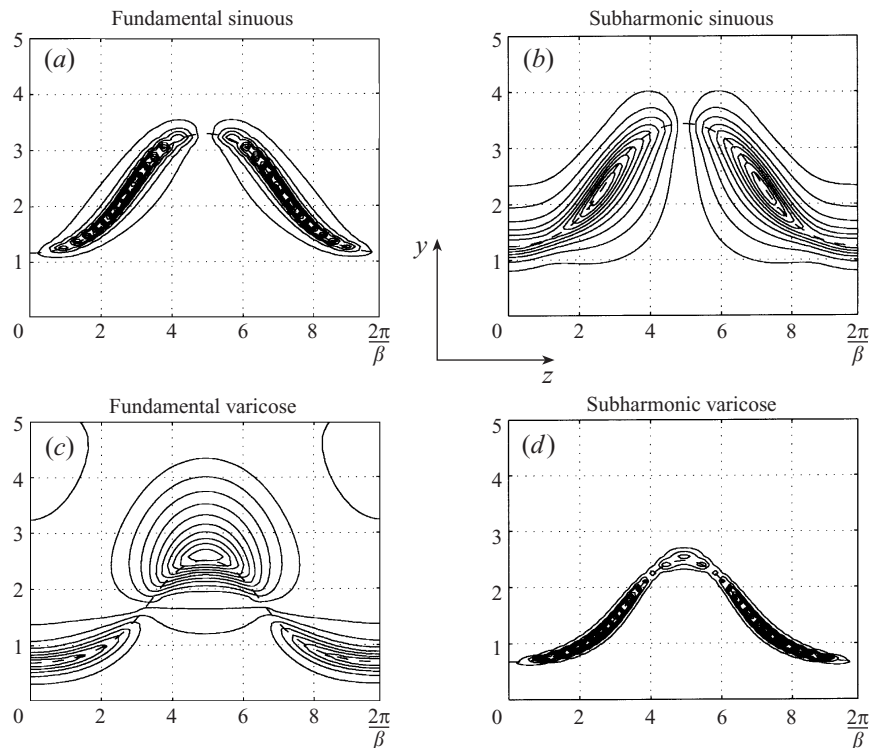
FIGURE 11. Contours of constant absolute values of the streamwise velocity component of four different kinds of modes obtained using the shape assumption. The dashed lines represent the contours of the constant value of the mean field corresponding to the phase velocities of the disturbances. The sinuous modes are calculated with parameters $\alpha = 0.150$, $\beta = 0.45$ and $A_s = 0.36$ at $x = 2$ (see figure 6a) ($c_r = 0.627$ and $\omega_i = 0.00301$ for the fundamental mode; $c_r = 0.661$ and $\omega_i = 0.0104$ for the subharmonic mode). The varicose modes are calculated with parameters $\alpha = 0.150$, $\beta = 0.45$ and $A_s = 0.38$ at $x = 2$ ($c_r = 0.379$ and $\omega_i = 0.00998$ for the fundamental mode; $c_r = 0.371$ and $\omega_i = 0.00297$ for the subharmonic mode). Note that the real and imaginary parts of the subharmonic modes have a period of $4\pi/\beta$. However, their absolute values are $2\pi/\beta$-periodic.

counterpart, but here the real and the imaginary parts of this u-eigenfunction are anti-symmetric around the axes $z = 0$ and $z = 2\pi/\beta$.

The fundamental u-eigenfunction displayed in figure 12(a) was obtained using the same mean field and streamwise wavenumber as the direct numerical simulations shown in figure 9(a). The agreement between figures 9(a) and 12(a) is very good and in fact, for this symmetry, there is also a fair agreement with the u-eigenfunction displayed in figure 11(a), which was obtained using the shape assumption. Also, the sinuous subharmonic u-eigenfunction 12(b) is in fair agreement with the one obtained using the shape assumption displayed in figure 11(b). In contrast, the fundamental and subharmonic varicose u-eigenfunctions are in poor agreement with both the u_{rms} plot of figure 10(a), obtained from direct numerical simulations, and the u-eigenfunctions of figures 11(c) and 11(d). As shown in figures 12(c) and 12(d) the u-eigenfunctions are considerably less diffuse and are strongly concentrated around the isoline $U = c_r$.

The growth rates of the varicose (fundamental and subharmonic) symmetries are highly over-predicted when the shape assumption is used. The positive growth rates of the fundamental varicose case are found to be even larger than those for the
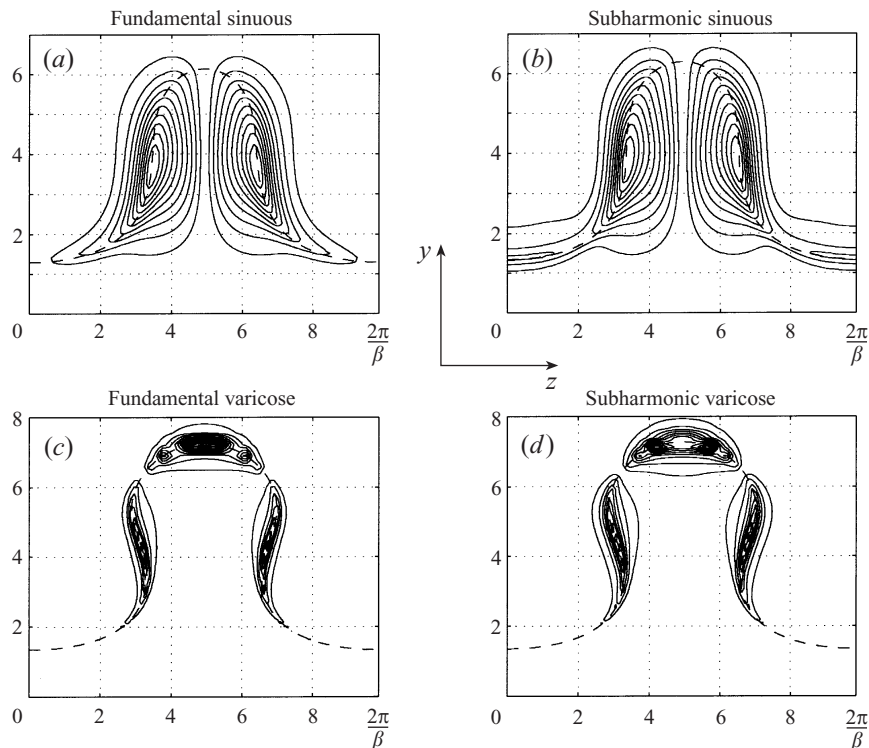
FIGURE 12. Contours of constant absolute values of the streamwise velocity component of four different kinds of modes obtained using the nonlinear mean fields. The dashed lines represent the contours of the constant value of the mean field corresponding to the phase velocities of the disturbances. The sinuous modes are calculated using the nonlinear mean field corresponding to the circled line in figure 5(a), at streamwise position $x = 2$, where $A = 0.36$, for a streamwise wavenumber $\alpha = 0.280$ ($c_r = 0.821$ and $\omega_i = 0.0144$ for the fundamental mode; $c_r = 0.839$ and $\omega_i = 0.0125$ for the subharmonic mode). The varicose modes are calculated using the mean field with largest streak amplitude (see figure 5b) at position $x = 2$, where $A = 0.378$, for a streamwise wavenumber $\alpha = 0.275$ ($c_r = 0.866$ and $\omega_i = 0.00218$ for the fundamental mode; $c_r = 0.876$ and $\omega_i = 0.00243$ for the subharmonic mode). In all calculations $Re_\delta = 430$ and $\beta = 0.45$.

fundamental sinuous case, which contradicts experiments and previous, comparable, calculations (Schoppa & Hussain 1997, 1998)

In comparing the mean fields obtained from the shape assumption to the fully nonlinear ones, we find that the inflection point in the wall-normal direction is smoothed by the nonlinear modification, cf. figure 13(a). This figure shows the streamwise velocity profiles centred on the low-speed streak (i.e. $z = \pi/\beta$) for the two types of mean fields and for a large amplitude. This z-location has been chosen since it is where a wall-normal inflection point first appears when the streak amplitude is increased, and also where the varicose eigenfunctions achieve their peak values. As reported in a number of experimental and numerical studies (Swearingen & Blackwelder 1987; Yu & Liu 1991; Le Cunff & Bottaro 1993; Bottaro & Klingmann 1996; Matsubara & Alfredsson 1998), the wall-normal inflection point can be related to the varicose mode, whereas sinuous instabilities correlate well with the spanwise mean shear.

The reason for the overpredicted varicose amplification factor when using the shape assumption can be deduced from inspection of figure 13: an inflection point
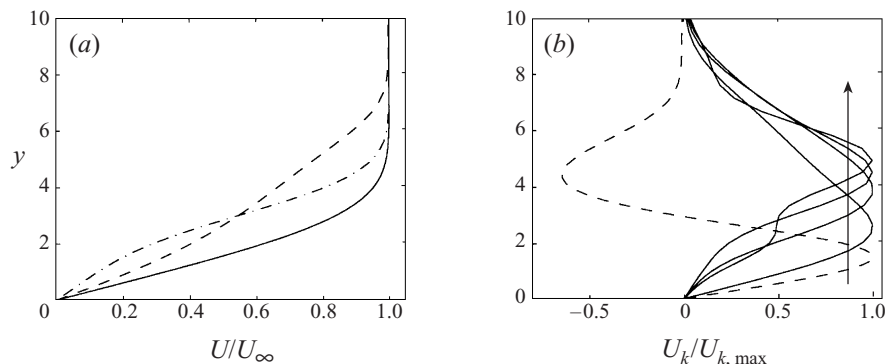
FIGURE 13. (a) The total streamwise velocity versus the wall-normal coordinate at $z = \pi/\beta$ for: - - - -, the nonlinear mean field, and -·--·-, the shape-assumption-approximated mean field. Here both amplitudes are $A = A_s = 0.33$, the streamwise position is $x = 2$ and the spanwise wavenumber is $\beta = 0.45$; the Blasius profile is drawn, for reference, with a solid line. (b) The different Fourier modes $U_k(y)$ representing the streamwise velocity of the nonlinear mean field in (a) versus the wall-normal coordinate. The dashed line corresponds to the mean flow distortion, $(U_0 - U_B)$, and the arrow points in the direction of higher-order modes. Every mode is normalized with its maximum $((U_0 - U_B)_{max} = 0.11, U_{1,max} = 0.26, U_{2,max} = 6.6 \times 10^{-2}, U_{3,max} = 1.1 \times 10^{-2}, U_{4,max} = 9.2 \times 10^{-4}.)$ Here $Re_\delta = 430$.

appears for y close to 3 in this case, but it disappears when the base flow contains all harmonics of the streak. Both the direct numerical simulations and the linear stability calculations using the nonlinearly distorted mean fields produce stable varicose modes for $A = 0.33$. In fact, only for the largest streak studied in this paper, corresponding to an amplitude $A = 0.373$, a slightly unstable varicose mode is found. The discrepancy in the secondary stability results between the two cases can be traced to the mean flow distortion $(U_0 - U_B)$ (see the dashed line in figure 13b). Calculations employing a 'nonlinear' mean field constructed without the mean flow distortion result in varicose perturbations with positive growth rates for $A = 0.33$.

Furthermore, the phase speed of the secondary instability is considerably increased when using the nonlinear mean fields. This can be deduced by observing that non-linearities 'move' the primary instability outwards from the wall. In figure 13(b) the individual Fourier modes from the cosine expansion of the nonlinear mean field from figure 13(a) are shown, normalized to unit value. Note that higher-order modes are displaced away from the wall. The phase speed of the secondary instability equals the mean field velocity at the critical layer, cf. figure 11. Therefore, as the critical layer is moved outwards, where the mean flow velocity is higher, the phase speed of the secondary instability is also increased.

4.2. *Parametric study*

In figure 5(b) the downstream amplitude development of streamwise streaks for a spanwise wavenumber $\beta = 0.45$ and for different initial amplitudes is shown. Most of the linear stability calculations are performed using the velocity fields with the amplitudes found at $x = 2$. This position was chosen since it is close to the point where the primary disturbance energy attains its maximum value.

According to the scaling property of the mean fields derived in §3.2, the results obtained for the parameters used in this section, $x = 2$ and $\beta = 0.45$, can be rescaled to apply for all values of β (see figure 8). This implies that a result from a secondary instability calculation obtained using a mean field corresponding to a point on the
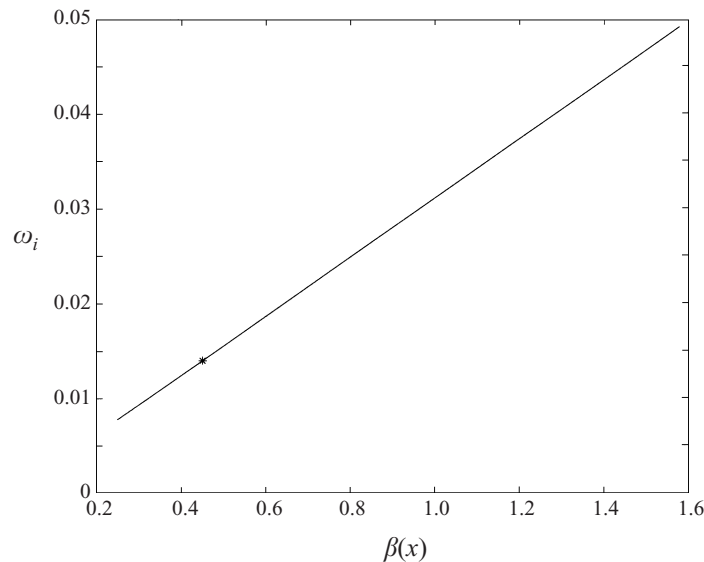
FIGURE 14. Results for the fundamental sinuous growth rates, ω_i, versus the spanwise wavenumbers along the curve in figure 8. The star gives the value of the amplification factor obtained when $A = 0.36$, $\alpha = 0.30$, $\beta = 0.45$ and $x = 2$, i.e. $\omega_i = 0.014$.

curve in figure 8 can be rescaled to yield the amplification value for all points on this curve. Since $\omega_i/\beta = $ constant, the value of the constant can be determined from a secondary instability result for a specific parameter combination. The line representing the growth rates of the fundamental sinuous symmetry is displayed in figure 14. In practice, however, the scaling property relating ω_i and β is limited to an intermediate range of β. Since their distance of amplification is so short, disturbances characterized by large values of β will need a large initial disturbance amplitude at the leading edge, whereas disturbances represented by low values of β will saturate far downstream, where Tollmien–Schlichting instabilities may become important and change the transition scenario. For larger values of β, the corresponding x-position is closer to the leading edge and viscous effects may have a damping influence on the amplification of unstable waves.

Primary disturbances with β in the range [0.3, 0.6] (here considered with respect to the fixed streamwise position $x = 1$), have the largest transient amplification (Andersson *et al.* 1999*a*; Luchini 2000). The spanwise distance selected in the controlled experiments by Bakchinov *et al.* (1995) corresponds to a value of β equal to 0.45 (at the location of their roughness elements), and this is also the scale of boundary layer fluctuations in the presence of free-stream turbulence (Westin *et al.* 1994). It could be speculated that this range of β is particularly appropriate when dealing with boundary layer streaks, since it corresponds to a spanwise spacing of about 100 wall units once viscous length scales are introduced. The spacing of 100 viscous wall units is not only obeyed by quasi-regular streaks in turbulent but also in laminar and transitional boundary layers (see Blackwelder 1983; Kendall 1985, 1990; Westin *et al.* 1994). It is also the typical transverse 'box' dimension for turbulence to survive in the minimal channel simulations of Jimenez & Moin (1991) and Hamilton, Kim & Waleffe (1995). In the present case, if a simple measure of the friction velocity is adopted by the use of the Blasius wall shear, it is easy to see that streaks spaced
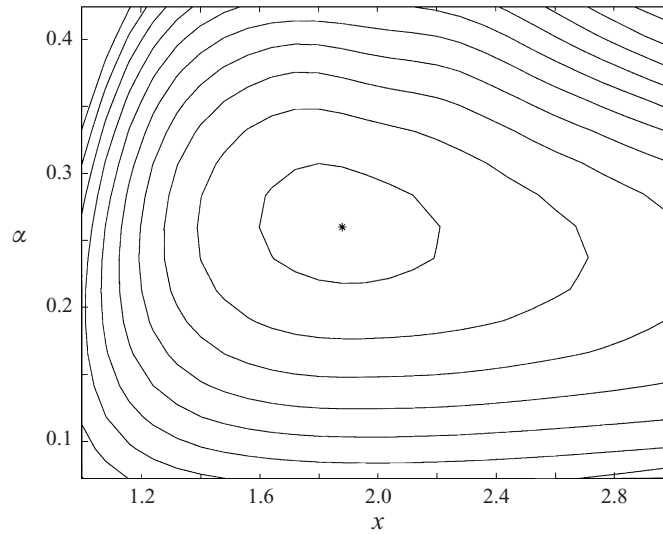
FIGURE 15. Isocontours of the growth rate ω_i, in the (x, α)-plane, for the sinuous fundamental mode, employing the mean field corresponding to the circled line in figure 5. The maximum contour level is 0.014 and the spacing is 0.0014. The $*$ represents the maximum growth rate, $\omega_i = 0.0147$, obtained at position $x = 1.88$ and for a streamwise wavenumber $\alpha = 0.259$.
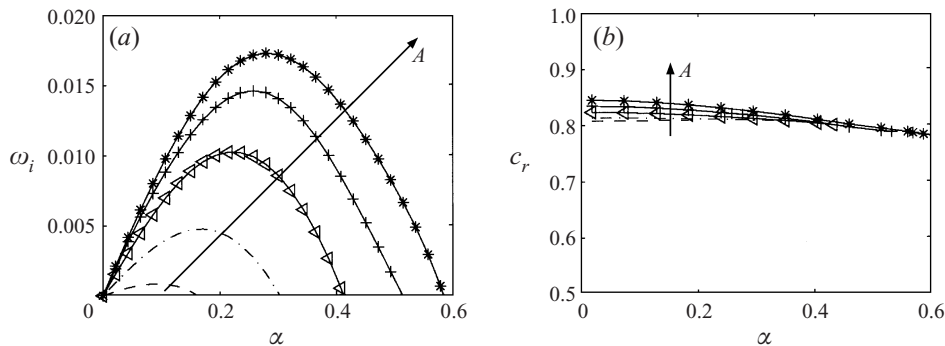

FIGURE 16. Temporal growth rate (*a*) and phase speed (*b*) versus streamwise wavenumber for the fundamental sinuous modes for different amplitudes of the primary disturbance (- - -, $A = 28.8$; -----, $A = 31.7$; —◁—, $A = 34.5$; —+—, $A = 36.4$; —∗—, $A = 37.3$). The arrows point in the direction of increasing A.

100 wall units apart are present in a subcritical (with respect to TS waves) boundary layer if β is in the range [0.3, 0.63].

Figure 15 shows the isocontours of the growth rate ω_i, for the fundamental sinuous instability in the (x, α)-plane for the mean field corresponding to the circled line in figure 5. The growth rates do not vary significantly for the range $1.6 < x < 2.2$ and, in this interval, the maximum growth rate is obtained for nearly the same value of the streamwise wavenumber ($\alpha = 0.259$). Stability calculations are, therefore, performed on the mean field at $x = 2$, where the primary disturbance has saturated and, for the cases with lower initial energy, the streak amplitude achieves its maximum value (cf. figure 5).

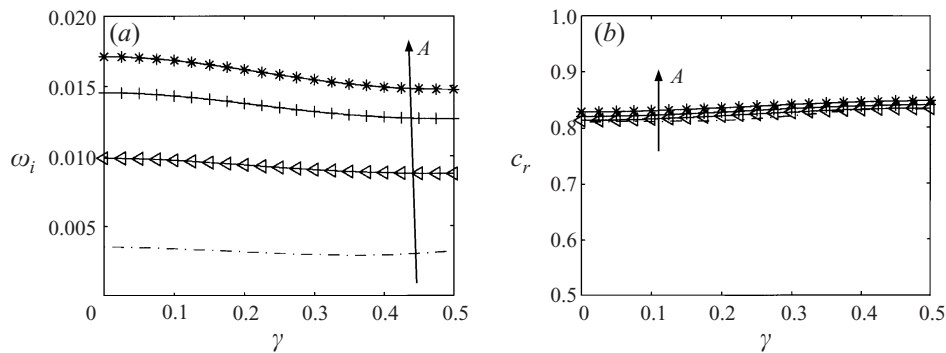An extensive parametric study is carried out for the sinuous fundamental ($\gamma = 0$),

FIGURE 17. Temporal growth rate (*a*) and phase speed (*b*) versus the Floquet parameter for sinuous modes, for four different amplitudes of the primary disturbance (symbols as in figure 16).

arbitrarily detuned ($0 < \gamma < 0.5$) and subharmonic ($\gamma = 0.5$) symmetries, which were the only ones found to be significantly unstable. First the Floquet parameter is set to zero, i.e. fundamental modes are focused upon. In figure 16(*a*) the growth rate of the instability $\omega_i = \alpha c_i$ is plotted against the streamwise wavenumber, for the different amplitudes of the streaks, obtained with the DNS. One can note that on increasing the amplitude, not only do the growth rates increase but their maxima are also shifted towards larger values of the streamwise wavenumber α. As shown in figure 16(*b*) the phase speeds of the fundamental sinuous modes are but weakly dispersive.

Next, we examine the effect of changes in the spanwise wavelength of the secondary disturbance, i.e. we study the effect of the detuning parameter γ. It is often assumed that the preferentially triggered secondary instability modes have the same transverse periodicity as the base flow; this is not at all evident here. The full system of equations (2.12)–(2.13) has been solved without resorting to symmetry considerations to yield the results displayed in figure 17, corresponding to a streamwise wavenumber α equal to 0.255 and for mean fields with amplitudes large enough to lead to instabilities for the chosen α. A monotonic behaviour is observed in the γ range of [0, 0.5] except for the case of lower amplitude A.

The behaviour of the amplification factor of the subharmonic modes for different streamwise wavenumbers and different amplitudes of the primary disturbance is shown in figure 18(*a*). For amplitudes larger than about 0.30, the subharmonic symmetry produces lower maximum growth rates than the fundamental symmetry. Note, however, that for lower amplitudes the sinuous subharmonic symmetry represents the most unstable mode. The phase speed for the subharmonic symmetry, displayed in figure 18(*b*), is larger than in the fundamental case and the waves are slightly more dispersive.

4.3. *The neutral conditions of streak breakdown*

A study has been conducted to identify the marginal conditions of breakdown, with each neutral point $\omega_i = 0$ calculated for a range of α by means of the complex integration technique discussed in §2.3. The steady base velocity profiles obtained with the DNS at $x = 2$ are used here. The results are displayed in figure 19(*a, b*) for the two sinuous symmetries, together with contour levels of constant growth rates.

It is immediately observed that a streak amplitude of about 26% of the free-stream speed is needed for breakdown to occur. Although this critical value is achieved for small values of α (where the parallel flow assumption becomes questionable) we
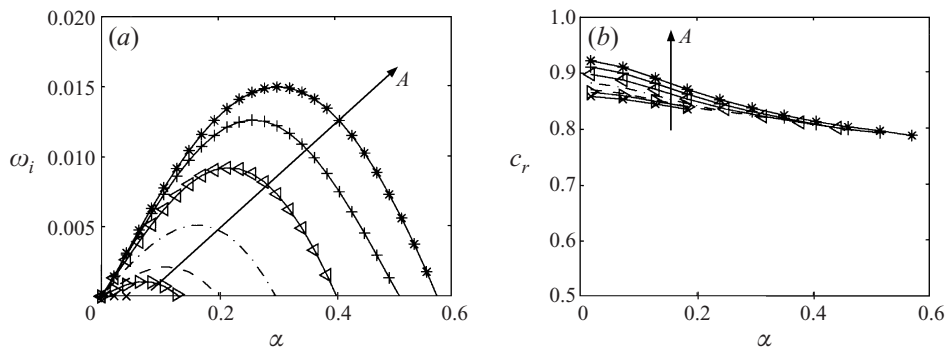
FIGURE 18. Temporal growth rate (*a*) and phase speed (*b*) versus streamwise wavenumber for the subharmonic sinuous modes for different amplitudes of the primary disturbance (—×—, $A = 25.6$; —▷—, $A = 27.2$; - - -, $A = 28.8$; ·····, $A = 31.7$; —◁—, $A = 34.5$; —+—, $A = 36.4$; —*—, $A = 37.3$).
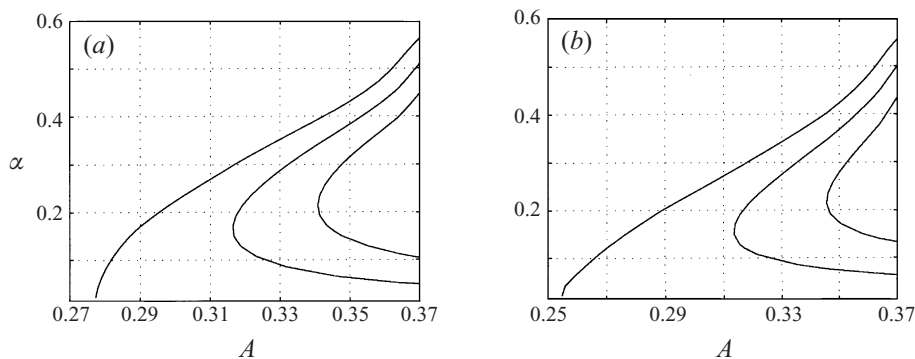

FIGURE 19. Neutral curves for streak instability in the (A, α)-plane for (*a*) the fundamental sinuous mode, (*b*) the subharmonic sinuous mode (contour levels: $\omega_i = 0, 0.0046, 0.0092$).

are roughly around the values reported by P. H. Alfredsson (private communication, 1998), who stated that "amplitudes of at least 20%" are needed for an instability of the streaks to emerge, and by Bakchinov *et al.* (1995) who in their experiments produced streaks with $A \approx 20\%$ and generated their controlled excitation with a vibrating ribbon. In the case of plane Poiseuille flow, the experiments of Elofsson *et al.* (1999) show that the threshold amplitude for streak breakdown is 35%, irrespective of the Reynolds number. This Reynolds-number independence was also observed in direct numerical simulations of Couette flow by Kreiss, Lundbladh & Henningson (1994) who reported that "the disturbances in the calculations are found to reach an amplitude of order one for all Reynolds numbers before the rapid secondary instability sets in".

One can notice that the subharmonic mode is unstable for lower amplitudes than the fundamental mode and that the growth rates for larger amplitudes are quite close for the two symmetries. The direct numerical simulations and experiments of oblique transition in a boundary layer conducted by Berlin, Lundbladh & Henningson (1994) and Berlin, Wiegel & Henningson (1999) show that a subharmonic breakdown of the streaks precedes transition to turbulence.

We do not present any results for the varicose instabilities here. In fact, both the fundamental and the subharmonic symmetries resulted in weak instabilities for

amplitudes larger than $A = 0.37$ with growth rates smaller than one fifth of the corresponding sinuous growth rates. Therefore a breakdown scenario triggered by a varicose instability seems unlikely.

It appears then that there is not a dominating mode but rather that fundamental and detuned sinuous instabilities have the same probability of being observed. Hence, the knowledge provided by these results must be combined with that of the inflow disturbance spectrum, i.e. the prevailing receptivity conditions. The present study furnishes possible scenarios which should be confirmed by careful experiments, i.e. with controlled harmonic disturbances to try and trigger specific modes.

5. Discussion and conclusions

We have investigated one of the mechanisms which is a possible precursor of transition to turbulence in a boundary layer, namely the linear instability of streaks produced by the non-modal streamwise evolution of free-stream disturbances. Such a breakdown has been observed in experiments carried out by the Swedish (Westin *et al.* 1994; Alfredsson & Matsubara 1996) and the Russian groups (Gulyaev *et al.* 1989; Bakchinov *et al.* 1995): they generated streaky structures and visualized their development, breakdown and the formation of turbulent spots, via smoke injection.

There is starting to be a good correspondence between experiments and theory, and most of the segments of transition induced by the breakdown of streaks are now elucidated (at least qualitatively). Our study aims at the modelling of only one part of this process. More complete pictures are starting to emerge, often based on simple model systems, particularly for the description of the self-sustained process that makes near-wall turbulence viable (for a recent account refer to the book by Panton 1997). Although similarities exist between the wall turbulence process and the breakdown of laminar streaks, it is best not to draw definite parallels because of the widely different space and time scales involved in the two cases.

Clearly, other steps can be envisioned to lead to early transition to turbulence (i.e. strong nonlinearities, resonant interactions, etc.) and the present work represents but one brick in the building of a comprehensive picture. One has to further appreciate the fact that in an actual experiment irregular streaky structures are often observed, i.e. with non-uniform spacing and with neighbouring streaks in different stages of development, see Bottin, Dauchot & Daviaud (1998) for an example in plane Couette flow. Thus, these structures do not necessarily become unstable together at a given x-position, but their breakdown will probably occur in an irregular manner. These aspects are linked to the flow receptivity, the understanding of which is, hence, crucial. For recent progress in this direction the reader is referred to Luchini & Bottaro (1998) and Airiau & Bottaro (1998).

The local, large Reynolds number limit has been considered here, with the implication that this simplified approach captures the essential features of the instability. The inviscid assumption means that one has to be careful in choosing the integration path for the eigenvalue calculation, and a simple procedure for identifying the singularities in the complex y-plane and for integrating around them has been outlined. With our approach, inspired by Lin (1944), neutral and damped inviscid modes can be computed, and a quasi-linear behaviour of the growth rate of the instability with the streak amplitude is found, in agreement with the careful channel flow measurements by Elofsson *et al.* (1999).

We have shown here that both the linear and the nonlinear spatial development of optimal streamwise streaks are well described by the boundary layer approximation

and, as a consequence, Reynolds number independent for large enough Reynolds numbers. This results in a boundary layer scaling property that couples the streamwise and spanwise scales, implying that the same solution is valid for every combination of x and β such that the product $x\beta^2$ remains constant. The parameter study of streak instability is therefore representative of a wide range of intermediate values of β for which saturation occurs at a reasonable x: large enough so that the boundary layer approximation may still be valid and small enough so that Tollmien–Schlichting waves may not play a significant role.

The different modes of instability have been catalogued and studied. At a preliminary stage secondary instability calculations of the shape-assumption-approximated mean fields were carried out; however, most results presented here are performed employing the fully nonlinear mean fields. In comparing the two levels of approximations we conclude that the shape assumption must be abandoned in secondary instability studies of streamwise streaks in flat-plate boundary layers. The secondary instability results are very sensitive to a slight change in the shape of the mean field velocity profile and, even if the sinuous modes are reasonably well captured by the shape assumption, the growth rates of varicose modes are widely over-predicted.

When considering the nonlinear mean field we find that the sinuous modes are by far the dominating instabilities. The varicose modes become unstable only for very large amplitudes (around 37% of the free-stream speed) and should, therefore, be rarely observed in natural transition. This is in agreement with DNS and experiments, where the sinuous modes of instability are most often reported for the streak breakdown.

Noticeable is the fact that the sinuous, detuned instability waves can be more amplified than the fundamental modes. The subharmonic modes are in fact found to first become unstable with a critical streak amplitude of about 26% of the free-stream velocity. Plots of the eigenfunctions for fundamental and subharmonic modes demonstrate clearly that the instability is concentrated around the critical layer, and both types of sinuous modes of breakdown are found to be almost non-dispersive. When the streak amplitude is large enough (around 30% of the free-stream velocity) both the fundamental and detuned modes have positive growth rates; thus, they might both be observed and to decide on their downstream fate is a matter of environmental bias. It is noteworthy that both experiments (Bakchinov *et al.* 1995) and DNS (Berlin *et al.* 1994) did show subharmonic breakdown of the streaks, although neither paper stated so explicitly.

Neutral curves have been obtained here in the amplitude–streamwise wavenumber plane; their identification should prove useful for controlling transition and near-wall turbulence.

Future experiments under controlled conditions may attempt to trigger some of the modes described here. Also, an interesting direction of future research concerns the search for a possible absolute instability of the streaks. Finding a self-sustaining instability mechanism could provide a firmer connection with the birth of turbulent spots.

REFERENCES

AIRIAU, C. & BOTTARO, A. 1998 Receptivity of Tollmien-Schlichting waves via adjoint PSE. Presented at the EUROMECH colloquium 380: *Laminar-Turbulent Transition Mechanisms and Prediction*, Göttingen, Germany, September 14–17, 1998.

ALFREDSSON, P. H. & MATSUBARA, M. 1996 Streaky structures in transition. In *Proc. Transitional Boundary Layers in Aeronautics* (ed. R. A. W. M. Henkes & J. L. van Ingen), pp. 373–386. Royal Netherlands Academy of Arts and Sciences. Elsevier Science Publishers.

ANDERSSON, P., BERGGREN, M. & HENNINGSON, D. S. 1999a Optimal disturbances and bypass transition in boundary layers. *Phys. Fluids* **11**, 134.

ANDERSSON, P., BOTTARO, A., HENNINGSON, D. S. & LUCHINI, P. 1999b Secondary instability of boundary layer streaks based on the shape assumption. *TRITA-MEK Rep.* 1999:13. Department of Mechanics, The Royal Institute of Technology, Stockholm, Sweden.

BAKCHINOV, A. A., GREK, G. R., KLINGMANN, B. G. B. & KOZLOV, V. V. 1995 Transition experiments in a boundary layer with embedded streamwise vortices. *Phys. Fluids* **7**, 820.

BAYLY, B. J., ORSZAG, S. A. & HERBERT, T. 1988 Instability mechanisms in shear flow transition. *Ann. Rev. Fluid Mech.* **20**, 359.

BERLIN, S. & HENNINGSON, D. S. 1999 A nonlinear mechanism for receptivity of free-stream disturbances. *Phys. Fluids* **11**, 3749.

BERLIN, S., LUNDBLADH, A. & HENNINGSON, D. S. 1994 Spatial simulations of oblique transition in a boundary layer. *Phys. Fluids* **6**, 1949.

BERLIN, S., WIEGEL, M. & HENNINGSON, D. S. 1999 Numerical and experimental investigations of oblique boundary layer transition. *J. Fluid Mech.* **393**, 23.

BERTOLOTTI, F. P., HERBERT, T. & SPALART, P. R. 1992 Linear and nonlinear stability of the Blasius boundary layer *J. Fluid Mech.* **242**, 441.

BLACKWELDER, R. F. 1983 Analogies between transitional and turbulent boundary layers. *Phys. Fluids* **26**, 2807.

BOBERG, L. & BROSA, U. 1988 Onset of turbulence in a pipe. *Z. Naturforschung* **43a**, 697.

BOIKO, A. V., KOZLOV, V. V., SYZRANTSEV, V. V. & SHCHERBAKOV, V. A. 1997 A study of the influence of internal structure of a streamwise vortex on the development of travelling disturbances inside it. *Thermophys. Aeromech.* **4**, 343.

BOTTARO, A. & KLINGMANN, B. G. B. 1996 On the linear breakdown of Görtler vortices. *Eur. J. Mech.* B/*Fluids* **15**, 301.

BOTTIN, S., DAUCHOT, O. & DAVIAUD, F. 1998 Experimental evidence of streamwise vortices as finite amplitude solutions in transitional plane Couette flow. *Phys. Fluids* **10**, 2597.

BUTLER, K. M. & FARRELL, B. F. 1992 Three-dimensional optimal perturbations in viscous shear flow. *Phys. Fluids* A **4**, 1637.

DAUCHOT, O. & DAVIAUD, F. 1995 Finite amplitude perturbation and spots growth mechanism in plane Couette flow. *Phys. Fluids* **7**, 335.

DRAZIN, P. G & REID, W. H. 1981 *Hydrodynamic Stability*. Cambridge University Press.

ELLINGSEN, T. & PALM, E. 1975 Stability of linear flow. *Phys. Fluids* **18**, 487.

ELOFSSON, P. A., KAWAKAMI, M. & ALFREDSSON, P. H. 1999 Experiments on the stability of streamwise streaks in plane Poiseuille flow. *Phys. Fluids* **11**, 915.

GASTER, M. 1962 A note on the relation between temporally-increasing and spatially-increasing disturbances in hydrodynamic stability. *J. Fluid Mech.* **14**, 222.

GULYAEV, A. N., KOZLOV, V. E., KUZNETSOV, V. R., MINEEV, B. I. & SEKUNDOV, A. N. 1989 Interaction of a laminar boundary layer with external turbulence *Izv. Akad. Nauk SSSR, Mekh. Zhid. Gaza.* **5**, 55 (in Russian, English transl. 1990 in *Fluid Dyn.* **24**:5, 700).

GUSTAVSSON, L. H. 1991 Energy growth of three-dimensional disturbances in plane Poiseuille flow. *J. Fluid Mech.* **224**, 241.

HALL, P. & HORSEMAN, N. J. 1991 The linear inviscid secondary instability of longitudinal vortex structures in boundary-layers. *J. Fluid Mech.* **232**, 357.

HAMILTON, J. M., KIM, J. & WALEFFE, F. 1995 Regeneration mechanisms of near-wall turbulence structures. *J. Fluid Mech.* **287**, 317.

HENNINGSON, D. S. 1987 Stability of parallel inviscid shear flow with mean spanwise variation. *Tech. Rep.* FFA-TN 1987-57. Aeronautical Research Institute of Sweden, Bromma.

HENNINGSON, D. S. 1995 Bypass transition and linear growth mechanisms. In *Advances in Turbulence V* (ed. R. Benzi). Kluwer.

HENNINGSON, D. S. 1996 Comment on 'Transition in shear flows. Nonlinear normality versus non-normal linearity' [Phys. Fluids 7 3060 (1995)] *Phys. Fluids* **8**, 2257.

HENNINGSON, D. S., LUNDBLADH, A. & JOHANSSON, A. V. 1993 A mechanism for bypass transition from localized disturbances in wall bounded shear flows. *J. Fluid Mech.* **250**, 169.

HENNINGSON, D. S. & REDDY, S. C. 1994 On the role of linear mechanisms in transition to turbulence. *Phys. Fluids* **6**, 2862.

HERBERT, T. 1988 Secondary Instability of boundary layers. *Ann. Rev. Fluid Mech.* **20**, 487.

HULTGREN, L. S. & GUSTAVSSON, L. H. 1981 Algebraic growth of disturbances in a laminar boundary layer. *Phys. Fluids* **24**, 1000.

JIMENEZ, J. & MOIN, P. 1991 The minimal flow unit in near wall turbulence. *J. Fluid Mech.* **225**, 221.

JIMENEZ, J. & PINELLI, A. 1999 The autonomous cycle of near wall turbulence. *J. Fluid Mech.* **389**, 335.

KENDALL, J. M. 1985 Experimental study of disturbances produced in a pre-transitional laminar boundary layer by weak free-stream turbulence. *AIAA Paper* 85-1695.

KENDALL, J. M. 1990 Boundary layer receptivity to free-stream turbulence. *AIAA Paper* 90-1504.

KIM, J., MOIN, P. & MOSER, R. 1987 Turbulence statistics in fully developed channel flow. *J. Fluid Mech.* **177**, 133.

KREISS, G., LUNDBLADH, A. & HENNINGSON, D. S. 1994 Bounds for threshold amplitudes in subcritical shear flows. *J. Fluid Mech.* **270**, 175.

LANDAHL, M. T. 1975 Wave breakdown and turbulence. *SIAM J. Appl. Maths* **28**, 735.

LANDAHL, M. T. 1980 A note on an algebraic instability of inviscid parallel shear flows. *J. Fluid Mech.* **98**, 243.

LE CUNFF, C. & BOTTARO, A. 1993 Linear stability of shear profiles and relation to the secondary instability of the Dean flow. *Phys. Fluids* A **5**, 2161.

LI, F. & MALIK, M. R. 1995 Fundamental and subharmonic secondary instabilities of Görtler vortices. *J. Fluid Mech.* **297**, 77.

LIN, C. C. 1944 On the stability of two-dimensional parallel flows. *Proc. Natl Acad. Sci.* **30**, 316.

LIN, C. C. 1955 *The Theory of Hydrodynamic Stability*. Cambridge University Press.

LUCHINI, P. 2000 Reynolds-number-independent instability of the boundary layer over a flat surface: optimal perturbations. *J. Fluid Mech.* **404**, 289.

LUCHINI, P. & BOTTARO, A. 1998 Görtler vortices: a backward-in-time approach to the receptivity problem. *J. Fluid Mech.* **363**, 1.

LUNDBLADH, A., BERLIN, S., SKOTE, M., HILDINGS, C., CHOI, J., KIM, J. & HENNINGSON, D. S. 1999 An efficient spectral method for simulation of incompressible flow over a flat plate. *TRITA-MEK Tech. Rep.* 1999:11. Royal Institute of Technology, Stockholm, Sweden

LUNDBLADH, A. & JOHANSSON, A. V. 1991 Direct simulation of turbulent spots in plane Couette flow. *J. Fluid Mech.* **229**, 499.

MALIK, M. R., ZANG, T. A. & HUSSAINI, M. Y. 1985 A spectral collocation method for the Navier–Stokes equations. *J. Comput. Phys.* **61**, 64.

MATSUBARA, M. & ALFREDSSON, P. H. 1998 Secondary instability in rotating channel flow. *J. Fluid Mech.* **368**, 27.

MORKOVIN, M. V. & RESHOTKO, E. 1990 Dialogue on progress and issues in stability and transition research. In *Laminar-Turbulent Transition* (ed. D. Arnal & R. Michel). Springer.

ORSZAG, S. A. & PATERA, A. T. 1983 Secondary instability of wall-bounded shear flows. *J. Fluid Mech.* **128**, 347.

PANTON, R. L. 1997 (Ed.) *Self-Sustaining Mechanisms of Wall Turbulence*. Computational Mechanics Publications, Southampton.

PARK, D. S. & HUERRE, P. 1995 Primary and secondary instabilities of the asymptotic suction boundary layer on a curved plate. *J. Fluid Mech.* **283**, 249.

RANDRIARIFARA, T. 1998 The instability of streamwise vortices in a curved, rotating channel. *Phys. Fluids* (submitted).

REDDY, S. C. & HENNINGSON, D. S. 1993 Energy growth in viscous channel flows. *J. Fluid Mech.* **252**, 209.

REDDY, S. C., SCHMID, P. J., BAGGETT, J. S. & HENNINGSON, D. S. 1998 On the stability of streamwise streaks and transition thresholds in plane channel flows. *J. Fluid Mech.* **365**, 269.

RESHOTKO, E. 1994 Boundary layer instability, transition and control. *AIAA Paper* 94-0001.

ROMANOV, V. A. 1973 Stability of plane-parallel Couette flow. Translated in *Functional Anal. Applics.* **7**, 137.

SCHOPPA, W. & HUSSAIN, F. 1997 Genesis and dynamics of coherent structures in near-wall turbulence: a new look. In *Self-Sustaining Mechanisms of Wall Turbulence* (ed. R. L. Panton), pp. 385–422. Computational Mechanics Publications, Southampton.

SCHOPPA, W. & HUSSAIN, F. 1998 Formation of near-wall streamwise vortices by streak instability. *AIAA Paper* 98-3000.

SWEARINGEN, J. D. & BLACKWELDER, R. F. 1987 The growth and breakdown of streamwise vortices in the presence of a wall. *J. Fluid Mech.* **182**, 255.

TILLMARK, N. & ALFREDSSON, P. H. 1992 Experiments on transition in plane Couette flow. *J. Fluid Mech.* **235**, 89.

TREFETHEN, L. N., TREFETHEN, A. E., REDDY, S. C. & DRISCOLL, T. A. 1993 Hydrodynamic stability without eigenvalues. *Science* **261**, 578.

USTINOV, M. V. 1998 Stability of streaky structures in boundary layer. Presented at the EUROMECH colloquium 380: *Laminar–Turbulent Transition Mechanisms and Prediction*, Göttingen, Germany, September 14–17, 1998.

WALEFFE, F. 1995 Hydrodynamic stability and turbulence: Beyond transients to a self-sustaining process. *Stud. Appl. Maths* **95**, 319.

WALEFFE, F. 1997 On a self-sustaining process in shear flows. *Phys. Fluids* A **9**, 883.

WESTIN, K. J. A., BOIKO, A. V., KLINGMANN, B. G. B., KOZLOV, V. V. & ALFREDSSON, P. H. 1994 Experiments in a boundary layer subject to free-stream turbulence. Part 1. Boundary layer structure and receptivity. *J. Fluid Mech.* **281**, 193.

YU, X. & LIU, J. T. C. 1991 The secondary instability in Goertler flow. *Phys. Fluids* A **3**, 1845.